

The mechanism of Mg diffusion in forsterite and the controls on its anisotropy

Joshua M. R. Muir^{* 1,2}, Feiwu Zhang¹ and Andrew M. Walker²

1) Institute of Geochemistry, Chinese Academy of Sciences, 99 West Lincheng Road, Guiyang, Guizhou 550081, China

2) School of Earth and Environment, University of Leeds, LS2 9JT, United Kingdom

*Corresponding author: j.m.r.muir@mail.gyig.ac.cn, a.walker@leeds.ac.uk, zhangfeiwu@mail.gyig.ac.cn

This is an Arxivpreprint which has not been peer reviewed. Previous versions of this paper included the effect of water on diffusion. Reviews have pointed out errors in our water calculation so those are being reviewed and revised. This version is being submitted to *Physics of the Earth and Planetary Interiors* for review.

The mechanism of Mg diffusion in forsterite and the controls on its anisotropy

Joshua M. R. Muir^{*1,2}, Zhang Feiwu¹ and Andrew M. Walker²

3) Institute of Geochemistry, Chinese Academy of Sciences, 99 West Lincheng Road, Guiyang, Guizhou 550081, China

4) School of Earth and Environment, University of Leeds, LS2 9JT, United Kingdom

*Corresponding author: j.m.r.muir@mail.gyig.ac.cn, a.walker@leeds.ac.uk, zhangfeiwu@mail.gyig.ac.cn

Abstract

Mg diffusion is important for explaining many deformational properties in forsterite but its mechanism is unknown and so the effect of variables such as pressure is difficult to constrain. In this study we used DFT to calculate the diffusion of Mg in forsterite. We predict vacancy diffusion to be highly anisotropic with considerably faster diffusion in the [001] direction while interstitial diffusion is predicted to be more isotropic. Thus we predict that a combination of interstitial and vacancy diffusion is required to reproduce experimentally derived anisotropies. Interstitial diffusion is predicted to be highly pressure dependant such that with increasing pressure the anisotropy of Mg diffusion decreases while temperature has little effect on this anisotropy. Substances like Fe and water likely cause increases in Mg diffusion rate through the creation of extrinsic Mg vacancies and we predict that without modifications to the inherent mobility of Mg vacancies these cause small increases to diffusional anisotropy at 1300 and 1600 K but very large increases at 1000 K.

Keywords: Forsterite; Mg Diffusion; DFT

1 Introduction

The importance of Mg diffusion in olivine

Diffusion of cations occupying the octahedral metal sites in olivine controls processes that are active in the Earth's crust and upper mantle, and which underpin a range of geophysical and geochemical techniques. In the upper mantle, where olivine with composition close to $(\text{Mg}_{0.9}\text{Fe}_{0.1})_2\text{SiO}_4$ is the dominant phase, the diffusivity of Mg is important in understanding electrical conductivity (Fei et al., 2018, Yoshino et al., 2009, Yoshino et al., 2017, Schock et al., 1989) and could influence deformation even though Mg is a rapidly diffusing species as argued in Jaoul (1990). Anisotropic Mg diffusion could be an important factor in explaining the anisotropic conduction seen in high conductivity layers underneath young oceanic plates (Fei et al., 2018) and, if Mg diffusion is important in forming olivine textures, could also help explain the variety of textures that are formed by olivine under different conditions (Karato et al., 2008). Mg-Fe interdiffusion occurring in zoned phenocrysts from volcanic products is increasingly used as a petrological tool (diffusion chronometry) to understand the timescales of pre-eruptive processes operating in the days and weeks prior to eruption (e.g. Hartley et al. 2016 and Pankhurst et al. 2018). On a longer timescale diffusion-controlled exchange between Mg and Fe in olivine and spinel can be used to infer the post-crystallisation thermal history of ultramafic igneous bodies (Ozawa, 1984). Diffusion can also lead to magnesium and iron isotope fractionation (Teng et al., 2011).

Our understanding and ability to model all of these processes relies on accurate determination of the Mg self-diffusion and Fe-Mg interdiffusion coefficients in olivine and thus this has been the focus of a range of experimental and computational studies reviewed by Chakraborty (2010). However, details of the atomic scale basis of Mg self and inter-diffusion in olivine have thus far eluded a full atomistic explanation and this limits our ability to confidently make use of this data under the wide range of conditions where diffusion is important. In this work we shall study the atomistic mechanisms of Mg self-diffusion as the more straightforward of these two processes.

Experimental measures of Mg diffusion

Previous studies have identified several key features of Mg self-diffusion as well as questions that remain unanswered. Despite early uncertainty, it is clear that magnesium self-diffusion is faster than the self-diffusion of oxygen or silicon (for a review of this history see Chakraborty (2010)). Diffusion can be described by a basic equation $D^{sd} = D_0 \exp\left(-\frac{E_{act}}{k_B T}\right)$ where D^{sd} is the rate of self-diffusion, D_0 is a preexponential factor, E_{act} is the activation energy, k_B is the Boltzmann constant and T is the temperature. These two values can then be treated as fitting factors for experiments run at different temperatures. Recent experimental estimates of E_{act} and D_0 for Mg tracer diffusion in forsterite are $9.6 \times 10^{-4} \text{ m}^2/\text{s}$ and $4.15 \pm 0.17 \text{ eV}$ (Chakraborty et al., 1994) or $4.0 \times 10^{-9} \text{ m}^2/\text{s}$ or $2.59 \pm 0.31 \text{ eV}$ (Fei et al., 2018). If we consider one set of parameters- 1300 K and 0 GPa the diffusion rate D of Mg is $3.6 \times 10^{-19} \text{ m}^2/\text{s}$ in Fei et al. (2018a) or $2-6 \times 10^{-19} \text{ m}^2/\text{s}$ in Chakraborty et al. 1994. In general, therefore, there is broad agreement as to the Mg diffusion parameters in dry forsterite though there is around half an order of magnitude discrepancy between different experimental predictions, some of which are plotted in Figure 5 (Andersson et al., 1989, Chakraborty et al., 1994, Fei et al., 2018, Jollands et al., 2020, Morioka, 1981) .

In detail, magnesium self-diffusivity is found to be mildly sensitive to pressure, to be anisotropic and to depend on the chemistry of the olivine crystal. There are some differences in experimental activation volumes $1-3.5 \text{ cm}^3/\text{mol}$ (Chakraborty et al., 1994) or $4.0-4.6 \text{ cm}^3/\text{mol}$ (Fei et al., 2018) but in all cases these are small and so pressure has little effect on diffusion rates. Diffusion along [001] has been found to be faster than diffusion along [100], which is faster than diffusion along [010] (Chakraborty et al., 1994) though other studies have found diffusion along [010] to be faster than diffusion along [100] (Andersson, 1987, Jollands et al., 2020).

Although these experiments provide the critical data needed to model diffusion-controlled processes in olivine, several aspects of Mg diffusion remain enigmatic and some parameters have not been fully established. For example, the reason for the anisotropy of diffusion is not clear and the effect of

pressure or other elements on this anisotropy has not yet been determined. An argument has been made that diffusional anisotropy is related to Mg hopping distance (Brodholt, 1997) but in a highly anisotropic crystal like forsterite the difficulty of Mg hopping is unlikely to be a simple function of distance. By using *ab-initio* calculations we can explore atomistic mechanisms by which these processes could occur.

Crystal structure of olivine

In order to understand diffusion in olivine it is necessary to consider the crystal structure, how this permits point defect mobility and the chemistry that controls the defect concentration. Olivine's distorted hexagonal close packed oxygen sublattice contains two distinct octahedrally co-ordinated M sites: M1, on an inversion centre, and the less symmetric M2, which sits on a mirror plane. M1 sites share edges and form continuous chains along [001] while M2 sites are isolated from each other (sharing an edge with an M1 site and corners with other M1 and M2 sites). This structural anisotropy hints at a possible reason for the directional dependence of Mg diffusion in forsterite: vacancy mobility along chains of M1 could be high compared to more tortuous pathways between M1 and M2 sites. There are also two normally unoccupied octahedral sites in the olivine structure. Each is located half way between two occupied M sites (and shares faces with them) along [100]. We call the unoccupied octahedral site midway between two M1 sites I1, and the unoccupied octahedral site midway between two M2 sites I2.

Theoretical Studies of Mg diffusion in Forsterite

Previous work has attempted to address the mobility of point defects in forsterite. Simulations using interatomic potentials (Wright and Catlow, 1994, Walker et al., 2009, Jaoul et al., 1995), density functional theory (Brodholt, 1997) and QM/MM embedded clusters (Walker et al., 2009) suggest that vacancies on the M1 site are more stable than vacancies on the M2 site, that octahedrally coordinated magnesium interstitials are unstable on I1 but can form on I2, and that a split-interstitial structure (two magnesium ions in tetrahedral coordination located on opposite sides of the M1 site) is stable

(Walker et al., 2009). The mobility of some of these defects has been studied using interatomic potentials (Bejina et al., 2009, Jaoul et al., 1995, Walker et al., 2009) where it was found that Mg vacancies are more mobile than Mg interstitials (Walker et al., 2009), that pressure has a limited effect on mobility along the M1 chain as was found in experiments (Jaoul et al., 1995, Bejina et al., 2009) and that vacancies overwhelmingly diffuse along the [001] M1 chain (Bejina et al., 2009). These studies have neglected important effects. First, interatomic potentials often behave poorly in unusual geometries and these are often formed during diffusion. Second, these studies consider only activation energies and not the time taken for diffusing point defects to overcome these barriers. And third, they do not convert their diffusion pathways into a macroscopic diffusion model and thus calculate rates of diffusion.

Thus there exists no detailed exploration of Mg diffusion in forsterite using electronic structure methods. In the following we make use of atomic scale simulation to understand the atomic scale mechanism of Mg diffusion in forsterite, determine the absolute diffusivity as a function of direction and how this is altered by pressure and how extrinsic defects could affect this picture.

2 Methods

Compared to the timescale accessible to direct atomic scale simulation using molecular dynamics, point defect diffusion in minerals is usually slow. Methods available to simulate diffusion thus seek to describe diffusion by repeated rare events which can be studied in detail, and then combined in order to describe diffusion on a meaningful timescale. The rare events are typically hops of point defects between adjacent sites. For example, one of a number of atoms could migrate into a vacancy, effectively moving the vacancy and permitting diffusion via a vacancy mechanism, or an interstitial atom could move into one of a number of different interstitial sites, permitting diffusion via an interstitial mechanism. Repeated occurrences of these hops leads to a random walk of the defect and bulk self-diffusion (Tilley, 1987). Our approach to simulating Mg diffusion in forsterite thus follows three steps. First, we make use of density functional theory to determine the structure and relative stability of stable Mg point defects in forsterite. These models represent the ground state end-points

of the hops leading to diffusion. Second, we probe the energy landscape that must be traversed by the defect during a hop. This provides us with the energy barrier that must be overcome for the hop to proceed and the structure of the transition state (the configuration with maximum energy on the minimum energy pathway between the start and the end point). Boltzmann statistics tell us how likely it is for a point defect to have enough energy at a given temperature to overcome the energy barrier while simulation of the lattice vibrations of the ground and activated state allow us to calculate the frequency at which each hop is attempted. Third, we combine information about multiple hops between different ground states using a kinetic Monte Carlo approach to access timescales long enough to observe the random walk and measure Mg diffusion in forsterite.

2.1 Defect calculations using density functional theory

All input parameters to our models of magnesium diffusion in forsterite are derived from atomic scale simulations. Specifically, we use a “planewave and pseudopotentials” approach (Payne et al., 1992), where density functional theory (DFT; Hohenberg and Kohn, 1964; Kohn and Sham, 1965) allows us to probe the energy of periodic boxes of simulated atoms. We use this to evaluate the ground state defect structures and energies, the structures and energies of the transition states, and the way atoms vibrate in these configurations. This approach allows us to calculate the hop activation energies and rates as a function of temperature and pressure. These calculations were undertaken using version 16.11 of the CASTEP code (Clark et al., 2005), which makes use of a plane wave basis for valence electrons (a cut off energy of 1000 eV was used throughout) and pseudopotentials to describe core electrons (on-the-fly ultra soft pseudopotentials were used with 2s, 3p and 3s, 2s and 2p, 3s and 3p, and 1s in the valence for Mg, O, Si and H, respectively). The PBE (Perdew et al., 1996) exchange correlation functional (a revised GGA functional) was used and, Kohn-Sham wavefunctions were represented on a (4x4x4) k-point grid in reciprocal space (Monkhorst and Pack, 1976).

We created models of Mg vacancies by removing an Mg²⁺ ion from an M1 or M2 site in a (2x1x2) forsterite super cell, with cell parameters fixed to those of the defect free crystal. Interstitial defects were created by inserting an extra Mg²⁺ ion into potential interstitial sites in the structure. To

account for atomic relaxation around the defects, the structure was then relaxed until the forces on all atoms were less than 0.01 eV/\AA and an energy tolerance of $1 \times 10^{-5} \text{ eV/atom}$ was repeated. Repeating calculations with increased cutoffs changed the energy of the supercell by $<0.1 \text{ meV/atom}$. A $(2 \times 1 \times 2)$ forsterite supercell was used to ensure that there was roughly 10 \AA between repeating vacancies in all directions, a distance we found to be sufficient to contain the important atomic relaxations. Simulation cells containing vacancies or interstitials have a net charge and so the energy calculated by CASTEP includes a defect-defect interaction term between adjacent supercells which does not reflect our desired energy of a charged defect in an infinite medium. We can approximately correct for this interaction by assuming it is the energy of a periodic array of point charges in a uniform neutralising background charge. This was done using the method of Leslie and Gillan (1985), first used for forsterite by Brodholt (1997). To use this method the relative permittivity of the cell needs to be set - we used a value of 6.2 (Weast, 1981). We repeated these calculations for a $(4 \times 2 \times 4)$ supercell containing a Mg vacancy, and the vacancy energy changed by $<0.01 \text{ eV}$, suggesting that our simulation cell size and energy corrections are sufficient for our needs.

Knowing the energy of defects allows us to calculate their population with assumptions about their formation reactions. The Mg Frenkel reaction ($Mg_{Mg}^X \rightarrow V_{Mg}'' + Mg_I^{\bullet\bullet}$) is the likely formation reaction for Mg vacancies (Dohmen and Chakraborty, 2007). This will be the source of defects in this work and the number of defects can be calculated from the knowledge of the defect energies of Mg vacancies and interstitials. This assumption is explored in the text.

Once ground state structures and energies for the defects had been determined, we enumerated the possible hops (where a defect moves from location to location) and for each hop we determined the pathway and found the transition state structure and energy. We did this by using a constrained optimisation approach. We first determined an approximate path for the hop (for vacancy diffusion this consists of two vacancies with a Mg atom at a point between the vacancies, for interstitial diffusion the interstitial atom is located between stable interstitial sites). For each hop we tried multiple paths, but direct paths proved to have the lowest transition state energy in all cases. A path

was defined by at least 10 images (with the Mg atom in different locations between the start and end point) and each image was relaxed with the migrating Mg fixed to the path by preventing its movement in one direction ([100] or [010] or [001]) with the fixed direction being that which has the longest distance along the path. This provides an energy profile along the path and a maximum energy point. We then searched for the transition state by moving along the path from the maximum energy point in 0.1 Å steps in both directions until a maximum was found. This is the candidate transition state. While this method may not definitely find the transition state our frequency calculations (below) typically returned a single imaginary eigenvalue of the dynamical matrix, as expected for a transition state. In the few cases, which were all for interstitial diffusion, where this was not the case the candidate transition state was found by manual adjustment based on visualising the eigenvectors of the imaginary phonon frequencies until a single imaginary eigenvalue was found. It turned out that this manual adjustment changed the activation energy of the hop by <0.01 eV suggesting that the constrained optimisation method is highly reliable for finding activation energies even if they are in complex parts of the energy hypersurface.

We repeated the calculations described above at 0, 5 and 10 GPa and 1000, 1300 and 1600 K by setting the simulation cell dimensions to minimise the Gibbs free energy of the defect free cell. The effect of pressure is easily accounted for by adding the PV term to the internal energy of the system. The effect of temperature requires consideration of the thermal motion of the atoms. We include this effect by making use of lattice dynamics to evaluate the phonon frequencies and then use these to evaluate the vibrational entropy of the crystal. Phonon frequencies were determined using the finite displacement method of CASTEP with finite displacements of 0.01 bohr. All lattice dynamics calculations were performed solely at the $q=(0,0,0)$ point. While this calculation at a single q-point may introduce a significant sampling error all of our calculations involve comparisons between two very similar structures- the start/end point of a diffusion step and its transition state- and so the effect of sampling errors are likely to be small but this is a limitation of the method. For lattice dynamics we tightened the convergence criteria on the forces and energy for the geometry optimisation to 0.001

eV/Å and 1×10^{-9} eV/atom, respectively- a few end points and transition states were sampled with 0.00075 and 5×10^{-10} eV/atom cuts off and the change in free energy caused by these increased cutoffs was <1 meV/atom. We determined the Gibbs free energy at a wide range of temperatures and at least 5 different volumes and then the energy at each volume with the following equations:

$$G(P, T, V) = U(V) + PV + E_{ZP}(V) - TS(T, V) \text{ Equation 1}$$

$$E_{ZP}(V) = \sum_{k,i} \frac{1}{2} \hbar \nu_{k,i}(V) \text{ Equation 2}$$

$$S(V) = - \sum_{k,i} \ln \left[1 - \exp \left(- \frac{\hbar \nu_{k,i}(V)}{k_B T} \right) \right] - \frac{1}{T} \sum_{k,i} \hbar \nu_{k,i}(V) \left[\exp \left(\frac{\hbar \nu_{k,i}(V)}{k_B T} \right) - 1 \right]^{-1} \text{ Equation 3}$$

Where $U(V)$ is the internal energy and $\nu_{k,i}(V)$ is the frequency of the phonon with wave vector k in the i -th band at volume V . At the pressure and temperature of interest the appropriate volume and energy was determined by fitting 2nd order polynomials across our volume range and minimising Equation 1. This method is quasi-harmonic as it ignores anharmonic effects beyond those caused by thermal expansion. Defected unit cells have different volumes than perfect unit cells. This effect is not large but to simulate the dilute limit we always used the lattice parameters of the perfect unit cell for defected unit cells.

2.3 From defects to diffusion

The self-diffusion of a Mg by a vacancy mechanism can be represented by:

$$D_{Mg}^{sd-vac} = D_{Mg}^{vac} N_{vac} \text{ Equation 4}$$

Where D_{Mg}^{vac} is the diffusion coefficient of Mg vacancies and N_{vac} is the atomic fraction of Mg vacancies.

As shown below, our atomic scale simulations suggest that diffusion of both interstitials and vacancies can be important for magnesium diffusion in pure forsterite. To account for this possibility we use the assumption that vacancies and interstitials diffuse independently of each other, which means that the total self-diffusion of Mg in forsterite is given by:

$$D_{Mg}^{sd} = D_{Mg}^{vac} N_{vac} + D_{Mg}^{Int} N_{Int} \text{ Equation 5.}$$

Other diffusing species (which are not considered in this paper) would have their own term if present. For systems with simple geometry, the diffusion coefficients can be found analytically from the attempt frequency, the migration entropy, the activation energy and the crystal structure. For example, for a single hop the coefficient is given by (Poirier, 1985):

$$D_{Mg}^{Vac} = \frac{\alpha}{q} l^2 v \exp\left(\frac{\Delta S_m}{k_B}\right) \exp\left(-\frac{\Delta H_m}{k_B T}\right) \text{ Equation 6}$$

where α is a geometric prefactor to account for the degeneracy of the hop, q is a dimensionality constant ($q = 2, 4$ or 6 for 1, 2 or 3D diffusion), l is the length of the hop and the two exponential terms are the migration entropy and the migration enthalpy, respectively. This approach has been used to determine diffusion coefficients in a number of minerals including MgO, bridgmanite and post-perovskite (e.g. Vocadlo et al. 1995; Ammann et al. 2010). However, forsterite diffusion involves defects moving from one site to an inequivalent site via multiple different hops and so it becomes cumbersome to attempt to develop equations of this type. Instead we seek a numerical estimate of the diffusion coefficients by implementing a kinetic Monte-Carlo (KMC; Bortz et al. (1975)) simulation of the motion of a defect in a forsterite crystal.

For our KMC method we need to know two things- the concentration of defects and the rate at which each Mg hop can occur. As explained above the concentration of intrinsic defects (vacancies and interstitials) were determined by minimising the free energy of the Frenkel reaction at the appropriate P and T.

To determine the rate of hopping we used lattice dynamics to probe the vibration of atoms around the point defects in their ground state and transition state configurations. This allows us to model the effect of temperature on point defect mobility. The rate, k , at which a defect hops from one location to another is given by:

$$k = v \exp\left(\frac{\Delta S_m}{k_B}\right) \exp\left(-\frac{\Delta H_m}{k_B T}\right) \text{ Equation 7}$$

where v is the attempt frequency (in Hz). The activation energy term was calculated from our constrained optimisation. In order to calculate the attempt frequency and activation entropy we used

Vineyard theory (Vineyard, 1957) which is based on absolute rate theory. Both of the temperature-based factors (vibrational entropy and attempt frequency) are combined into a modified attempt frequency which is found from the ratio of the calculated phonon frequencies:

$$v = \left(\frac{\prod_{j=1}^N v_j}{\prod_{j=1}^{N-1} v_{j'}} \right) \text{ Equation 8}$$

where v_j are the lattice frequencies of a defect in its stable starting position and $v_{j'}$ are the real lattice frequencies of the defect at the transition state of its hop. The latter has one imaginary frequency and so one less real frequency. As with our QHA method this theory assumes a harmonic approximation since motions near the saddle point are treated with the theory of small oscillations. Once activation energies and modified attempt frequencies have been calculated for each hop (and at each temperature and pressure of interest), we can calculate the rate of each hop and have all the atomic scale information in hand to evaluate the absolute diffusivity of magnesium in forsterite. These single hop parameters are then fed into our KMC algorithm.

First developed to allow the efficient simulation of Ising spin systems, KMC works by simulating the time evolution of a system between a collection of states, with transitions between states governed by a set of rules that includes a probability of that transition occurring in a given amount of time. Transitions between states are selected randomly (preserving the relative probability of each transition) and a clock is advanced by an appropriate amount after the state transition has been determined. This makes it useful for simulating complex transitions with many possible motions as the energetics of each motion can be calculated independently and then put collectively into a KMC algorithm. KMC has found a number of applications in extending atomic scale simulations to macroscopic behaviour, including the simulation of dislocation motion (Bulatov and Cai, 2006), chemical vapour deposition (Bagatur'yants et al., 2003) and point defect diffusion (Voter, 2007).

For our simulations, we followed the rejection-free residence time method of Voter (2007). A brief overview of this method shall be given with more detail in the Supplementary Information. For each

state in the system (eg a vacancy on M1) we enumerate all possible hops from that state and then calculate the rate of each hop (k^i) (equation 7 using equation 8), the sum of the rates of all the hops (k^{tot}) and the probability of each hop occurring $p^i = \frac{k^i}{k^{tot}}$. We then use the weighted probability of each hop to randomly select a hop. We also randomly select a time for that hop to occur (escape time) using Equation 9:

$$t^i = -\left(\frac{1}{k^{tot}}\right) \ln(r^2) \text{ Equation 9}$$

Where r^2 is a random number between 0 and 1. At each stage of the calculation the randomly selected hop moves our defect a certain distance in a certain direction and the randomly determined escape time advances the clock. Thus as this algorithm progresses, we build a list of positions of the defect as a function of time as it undergoes a random walk through the (infinite) crystal structure. We then can calculate the mean-squared displacement (MSD) of our defect (using the method of Leetmaa and Skorodumova (2015) as explained in the supplementary information) as a function of time. This can then be converted to diffusion using Equation 10:

$$\langle x^2 \rangle = qDt \text{ Equation 10}$$

Where q is the dimensionality constant as above.

2.4 Pressure correction

While DFT generally reliably reproduces pressure derivatives, the absolute pressures calculated by DFT are known to be systematically incorrect in that they are shifted in one direction. This arises as we use an approximation of the exchange-correlation term. As pressure differences are reliably reported (as the effects of the approximation largely cancel out) replication of experimental elasticities has been performed via simple correction schemes based on experimental volume and elasticity values. The most simple such method is a linear correction (Zhang et al., 2013), :

$$P(V, T) = P^{DFT}(V, T) - P^{DFT}(V_0^{exp}) \text{ Equation 11}$$

Where the subscript 0 represents the value of a parameter at a reference volume. Using a V_0^{exp} of 290.22 \AA^3 (Downs et al., 1996) we determined that our DFT values should be corrected by a value of -3.95 GPa . Such a correction allows us to recover experimental volumes across our pressure range (Table S1).

Some problems remain however. Such pressure correction methods have been benchmarked against experimental elasticities but it is unclear if such methods will work to correct defect energies and diffusion rates. These properties are strong functions of volume and thus likely do respond in such a way but we are not aware of any benchmarking done on this method. The choice of V_0 is also important. If V_0^{exp} is set to 287.4 \AA^3 (Isaak et al., 1989) then the pressure correction becomes -4.95 GPa . Thus we stress that our absolute pressures could have significant error in them but the relative effect of pressure on our model should be much more accurate. Due to this uncertainty we shall generally report uncorrected pressures.

3 Results

3.1 Defect Energies and Concentrations

There are two sites for Mg vacancies in forsterite – the M1 and the M2 sites. M1 sites are strongly favoured over M2 sites with pressure increasing the vacancy preference for M1 sites (Table S2). This preference for M1 over M2 vacancies agrees with previous calculations though there is some difference in the energy of this preference ($\sim 1.9 \text{ eV}$ with forcefield calculations (Walker et al., 2009) or $\sim 0.8 \text{ eV}$ using DFT (Brodholt, 1997)).

We have also considered Mg interstitials. As with Walker et al. (2009) we found that the most stable position is a split interstitial at the M1 site with 2 Mg atoms displaced from the centre of this site in opposite [010] directions (shown in Figure S1). This arrangement is very stable with alternative arrangements of the Mg at this site all relaxing into this one. Even placing a Mg atom in an I1 site causes it to relax into this split interstitial arrangement. The other stable configuration is found by placing an additional Mg in the I2 site. The Mg interstitial in the I2 site has an octahedral coordination

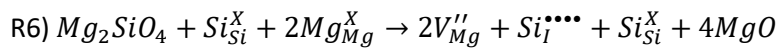
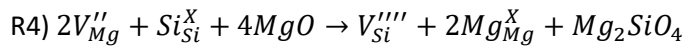
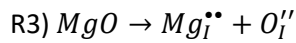
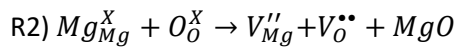
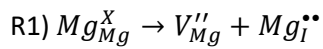
like the M1 and M2 and is thus geometrically similar to them. At 0 GPa the split M1 interstitial is slightly favoured over the I2 arrangement (~0.2 eV) but with increasing pressure the I2 configuration is favoured (Table S2) as the split M1 arrangement is larger than the I2 arrangement. This is in contrast to QM-MM embedded cluster calculations where this difference was found to be very large with an M1 geometry favoured over an I2 geometry by ~4.4 eV (Walker et al., 2009). It is also in contrast with our own forcefield calculations where we were unable to stabilise an I2 arrangement as I2 arrangements always relaxed into M1 arrangements. Forcefields are thus likely poor at calculating these interstitial structures.

To calculate diffusion rates the concentration of vacancies is required (Equation 5). For intrinsic diffusion we have assumed this comes from minimising the free energy of the Frenkel reaction ($Mg_{Mg}^X \rightarrow V_{Mg}'' + Mg_I^{**}$). When this reaction proceeds forward the positive enthalpy and the negative configurational entropy term both increase and at some concentration this provides a minimum energy. As the Mg interstitial is able to occupy two sites solving analytically for the free energy minimum is awkward. Instead we calculate the number of different arrangements of Mg vacancies and defects in the crystal considering all M1, M2, I1 and I2 sites and then calculate the probability of their occurrence and thus their configurational entropy. The steps for this are given in the supplementary information but the final result is that the equilibrium concentration in the intrinsic case comes from minimising Equation 12:

$$\Delta G = \Delta E \times a - TS_{confa} \text{ Equation 12}$$

where a is a reaction vector for the Frenkel reaction (between 0 and 1), ΔE is the energy of the Frenkel reaction and S_{confa} is the configurational entropy after the reaction has proceeded forward by a . The results of this minimisation are given in Table 1. Pressure strongly decreases the number of defects (by increasing the positive formation energy) whereas temperature increases the number of defects (as the configuration entropy is multiplied by $-T$).

To test the assumption that only the Frenkel reaction is important we looked at the following intrinsic reactions that produce Mg defects:



To simulate the other defects we probed all likely sites, found the sites with the minimum enthalpy and then calculated their high temperature energy through Equation 1-3. More details of the structures of these defects shall be provided in future work. The energy of these reactions is shown in Table S3 but all reactions have substantially higher energies than the Frenkel reaction (R1). By including these other reactions, which also compete in configurational entropy space, we change the concentration of Mg defects by less than 0.001% and thus these can safely be ignored and we shall only consider the Frenkel reaction R1 from now on.

3.2 Vacancy Hops

For Mg diffusion by vacancy hopping we found six different vacancy diffusion hops for which we calculated the geometries and energies of hopping. The hops that we have considered are shown and labelled in Figure 1 with their dimensions listed in Table S4 and described in the SI.

The activation energies and frequencies of these hops are presented in Table 2 and the barriers to diffusion are shown in Figure 2. Notably the A hop which is directly along the [001] direction has a substantially lower activation energy than all other M1 hops. The easiest hop from an M2 site is the C hop back to an M1 site. These two effects combine such that vacancies will diffuse easily along the [001] direction when in a M1 site and will have difficulty escaping to an M2 site. If they do escape to

an M2 site they will be converted quickly back to an M1 site. The weighted probability of these hops is shown in Figure 2 and an alternative representative in Figure S2 demonstrating the overwhelming dominance of the A hop.

Comparing our activation energies to published values we find that our value for the favoured A hop of 0.75 eV is similar to literature values of 0.72 (Walker et al., 2009) and 0.62 eV (Bejina et al., 2009). Our other hops have some variation with those found in Walker et al. (2009). To test whether this was an effect of simply using DFT as against using forcefields we recalculated our results using GULP with a TBH1 forcefield (Wright and Catlow, 1994) (Table S5, computational details in supplementary information). We find that generally DFT produces lower barriers than forcefield calculations but that the order of the hops is the same with both DFT and forcefield calculations. Crucially the activation energy of the easiest A hop (which largely controls the overall diffusion) is very similar with both methods 0.77/0.75 eV which means that both DFT and forcefield calculations return a very similar diffusivity for anhydrous vacancy diffusion.

We also considered the effect of pressure on the activation energies of these vacancies. As shown in Table S6 and Table S7 going from 0 to 10 GPa makes negligible differences to the activation energy or ν of any of the hops. The small differences seen are miniscule compared to the effect pressure has on the vacancy concentration as described above.

3.3 Mg interstitial hops

As Mg interstitials occupy M1 and I2 sites- the latter of which are simply shifted M2 sites- the geometry of interstitial hops are identical to those of vacancies. These hops are pictured and labelled in Figure 3 and their barriers in Figure 4 (and tabulated in Table S8) with their energies and frequencies in Table 3. The probability of any of the hops occurring is shown in Figure 4 and alternatively in Figure S3. These are again described in the supplementary information.

Interstitial hops I and J, which are between M1 and I2 sites, are the most favourable with energies <0.6 eV. In part this is because in the split M1 configuration one Mg at the M1 site is already close to an I2 site. Pressure has a small effect on the attempt frequency (Table S7) but a relatively large effect

on the activation energy of these hops (Table S9) with hop I becoming nearly barrierless by 10 GPa. Interstitial hops from the split M1 configuration have considerably lower attempt frequencies than the typical values between 1×10^{-12} and 1×10^{-13} Hz whereas hops from the I2 site show more typical attempt frequencies.

3.4 Diffusion

Using our KMC algorithm we can convert hops into diffusion rates. The diffusion coefficients for both vacancy and interstitial hopping are presented in Table 3 (these are listed at 5 and 10 GPa in Table S8 and S9). Vacancy diffusion is highly anisotropic with diffusion along [001] being orders of magnitude faster than diffusion along [100] or [010]. This is an outcome of diffusion where the hop directly along [001] is ~ 0.75 eV easier than any other M1 hop. In the absence of any additional undiscovered hops/mechanisms this will always hold. Interstitial diffusion is much more isotropic than vacancy diffusion due to the favourability of M1 to I2 hops (I and J) which go in all three primary directions.

To calculate total diffusion of Mg in forsterite we added together the rates of Mg vacancy and interstitial diffusion. This assumes that Mg Frenkel pairs are not associated with each other. To test this assumption we calculated the binding energy of this pair by running separate simulations with isolated Mg vacancies and interstitials and then calculations with them adjacent in the same unit cell and comparing the difference in enthalpy. We find that the binding energy is approximately -1.9 eV with a negative number indicating that bound defects are more stable than unbound defects. This is a large number but it is much smaller than the configurational energy gains of randomly scattering Mg vacancy and interstitial pairs for low concentrations. For the pairing energy to exceed this configuration entropy, the defect concentration would need to be above 1.2×10^{-3} defects per unit cell at 1300 K, many orders of magnitude larger than the predicted vacancy concentrations (Table 1). Thus the Mg vacancy and interstitial pairs are unlikely to be associated with each other and can be modelled individually here.

Figure 5 compares our pressure corrected results with some experimental measures of Mg self-diffusion at 0 GPa. We only plotted results for experiments buffered with MgO because enstatite has been observed (in one case) to increase Mg diffusion rates by nearly 1 order of magnitude (Jollands *et al.*, 2020). For Chakraborty *et al.* 1994 we plotted the results without buffer as the SiO₂ activity of these experiments is likely controlled by MgO (Jollands *et al.*, 2020). In the [001] direction our results are very similar to those of Jollands *et al.* 2020. The absolute value of our results, however, is somewhat unreliable as it is largely dependent on the choice of V_0^{exp} and thus the pressure correction. This is shown in Figure S4 where a larger (-5 GPa) pressure correction was applied and we find diffusion rates in the [001] direction very similar to those of Chakraborty *et al.* 1994. The results presented in Figure 5 use what we consider the most reliable pressure correction. Regardless our calculated [001] diffusion lies in the experimental range. In the [100] and [010] direction our results are within the experimental scatter of Andersson *et al.* (1989) but not that of Jollands *et al.* 2020. The experimental results have considerable differences from each other. While partly this is due to self-diffusion experiments being very difficult there is another possible cause. The most likely cause of these discrepancies is the presence of different extrinsic defects across different systems. Different extrinsic defects even if they do not diffuse themselves could vary the N_{vac} and N_{int} terms in Equation 5 and thus vary the diffusion rate. Such a variation would only have a very small effect on the experimentally determined activation energy unless the extrinsic defects were themselves produced thermally. Traditional measures of crystal purity are not adequate to accurately judge this effect as the key parameter is not so much the presence of different extrinsic defects but how these defects affect the intrinsic defects on a sub ppb level. To fully address this a large thermodynamic model needs to be built which is beyond the scope of this work. Another possibility is that there exists some factor of diffusion- such as an additional method of defect production- that is not replicated in this study. Our ability to replicate the results of Jollands *et al.* (2020) suggests that our model for diffusion in anhydrous forsterite accurately captures its diffusion in at least one case. Critically if interstitials are

not included in our model while [001] diffusion can be modelled accurately, [100] and [010] diffusion would be orders of magnitude slower than has been observed by any experiment.

We next consider the effect of pressure. Figure 6 shows our anhydrous [001] diffusion rates (with values listed in Table S10) as a function of pressure. Notably we find a larger pressure derivative for intrinsic diffusion coefficients than has been seen in the literature (Chakraborty et al., 1994, Fei et al., 2018). Our activation volumes are 6.69 cm³/mol at 1000 K, 7.51 cm³/mol at 1300 K and 7.84 cm³/mol at 1600 K. The pressure dependence of diffusion is strongly controlled in our case by the pressure dependence of defect concentration (Table 1) with little effect of the defect mobility (Table 3). Small changes to the formation energy of the Frenkel defect can have a strong effect on this dependence. If the number of defects is held constant across pressure then the calculated activation volumes are much smaller, ranging from -0.30 to 0.15 cm³/mol. These lower activation volumes are of relevance for cases where pressure does not alter the number of vacancies. For example, in an extrinsic regime (where vacancies form to charge balance impurities) the vacancy concentration is not temperature or pressure dependent and only the direct effect of pressure on vacancy mobility is important. In a real crystal with few impurities there will be a balance between the number of vacancies formed intrinsically via Frenkel pairs and the number of vacancies associated with impurities. In such a case, the effective activation volume will fall between our high and low values as is observed experimentally.

4. Discussion

4.1 Anisotropic intrinsic diffusion

One of the most notable features of our results is that Mg diffusion can be strongly anisotropic. Figure 7 shows the anisotropy of this diffusion as a function of pressure. We find that anisotropy decreases with pressure due to the increasing importance of interstitial diffusion, which is less anisotropic, with pressure while temperature has little effect on anisotropy. At 1600 K and 0 GPa (corrected) we find

that the ratio of diffusion in different directions [001]:[100] should be ~ 15 and [001]:[010] should be ~ 6 . Experimental measures of these ratios have produced lower results with [001]:[100] having values of ~ 3 (Chakraborty et al., 1994), 3.5-7 (Jollands et al., 2020) 7-40 (Andersson, 1987) and [001]:[010] having values of 4.5 (Chakraborty et al., 1994) 1.5-3.5 (Jollands et al., 2020) and 5-13 (Andersson, 1987). These experimental measurements were all at ambient pressures. Our calculated values for diffusional anisotropy are somewhat larger than has been seen experimentally. Our pressure correction method has not been calibrated for defect production and mobility and if the pressure correction was somewhat larger our anisotropies would approach the experimental range albeit its top end. One possible way to reduce the anisotropy would be to increase the ratio of Mg interstitials to Mg vacancies which could occur in the presence of extrinsic sources of Mg interstitials or chemicals that fill Mg vacancies. Alternatively, there could be some macroscopic effect that reduces diffusional anisotropy in real crystals and that we do not model.

Another issue is the order of diffusional speeds in different directions. Our calculations and some experiments (Andersson et al., 1989, Jollands et al., 2020) predict diffusion rates to be ordered [001]>[010]>[100] while Chakraborty et al. (1994) measured diffusion rates to be [001]>[100]>[010]. We do not have a source for this discrepancy as in our model both [010] and [100] diffusion are almost entirely controlled by interstitial I and J hops and thus their relative rate is fixed by the geometry of the crystal and not by any variable parameter. We have no hops that could selectively increase the [100] diffusion rate that are even close to being viable. Thus the presence of evidence suggesting that diffusion along [100] can be faster than diffusion along [010] suggests some kind of atomistic or macroscopic effect that is not being modelled in our system.

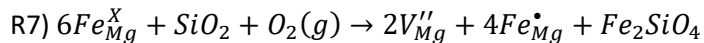
4.2 Anisotropy Changes in the Upper Mantle

While the dependence of anisotropy on pressure is large this probably has little implication in the upper mantle. After applying pressure corrections a 0-10 GPa range in the upper mantle would be equivalent to ~ 4 -16 GPa in our pressure scales. The largest changes in anisotropy come at the lowest

pressures and so across the pressure range of the upper mantle changes in Mg diffusional anisotropy with depth will typically be up to an order of magnitude except at the coldest temperatures (1000 K) where this could reach 1.5 orders of magnitude. These changes are likely to be too small to have any major effects on mantle rheology that change with depth.

4.3 The effect of extrinsic vacancies

Other substances such as iron (Chakraborty, 2010, Dohmen et al., 2007, Dohmen and Chakraborty, 2007) or water (Fei et al., 2018) that are in olivine can substantially change the diffusion rate. Without substantial changes to the diffusion mechanism there are two ways this can happen 1) through modifying the concentration of defects (N_{Vac} , N_{Int}) or 2) through modifying the mobility (D_{Mg}^{Vac} , D_{Mg}^{Int}) of defects. All substances that modify the diffusion rate likely do the former while only some do the latter. Iron can increase the number of Mg vacancies through the following reaction R7 (Dohmen and Chakraborty, 2007, Chakraborty, 2010):



whereas water can produce $(2H)_{Mg}^X$ vacancies. R7 has been invoked as the controlling reaction in Mg diffusion at intermediate temperatures in what is known as the Transition Metal Extrinsic Domain (TAMED) (Chakraborty, 2010). In the Fe-Mg interdiffusion case the mobility of vacancies is also modified as they include Fe self-diffusion coefficients and the cross section of Fe and Mg vacancy concentrations. In the case of water the mobility of $(2H)_{Mg}^X$ will be different to V_{Mg}'' but likely similar. In these and other cases we expect the change in the concentrations of vacancies to generally outweigh the changes to the mobility of vacancies due to the small number of intrinsic defects produced by the Frenkel reaction (Table 1). Extrinsic Mg vacancy concentration can be many orders of magnitude higher than intrinsic Mg vacancy concentration in many systems. This is seen in iron-containing olivine (Dohmen and Chakraborty, 2007) where the Mg vacancy concentration is many

orders higher than predicted here due to R7. Thus the prime reason that various contaminants cause an increase in Mg diffusion rates is likely to be the production of more Mg vacancies.

Critically Mg vacancies can be produced in this way but producing extrinsic Mg interstitials is much more difficult. Mg vacancies can be produced by many contaminants whereas Mg interstitials can only be produced by sources of Mg. This means that extrinsic defects are likely to produce a strong imbalance in the Mg vacancy vs Mg interstitial ratio.

This is explored in Figure 8 where we plot how increasing the diffusion rate solely by adding Mg vacancies changes the anisotropy of diffusion. There is an important caveat that this figure is constructed solely by changing defect species concentration and not the mobility of defects which will change somewhat in all real systems. Within this framework, however, we find that at lower mantle temperatures (1300, 1600 K) adding extrinsic defects has only small effects on the diffusional anisotropy. When diffusion rates match the measured diffusion rate of samples with likely amounts of Fe (1-20%) and water (1-100 ppm) diffusional anisotropy increases by 2-5 times at 1300 K and 5-10 GPa (uncorrected) and by less than 1.2 times at 1600 K in the same conditions. At lower temperatures, however, this increase in anisotropy can be much larger and can be >500 times at 1000 K. Lower temperatures will always have larger changes in anisotropy from extrinsic defects but the effect of extrinsic defect changes to mobility will also become more important at these lower temperatures and so our simple model will start to break down. Regardless at mantle relevant temperatures we observed only small changes in anisotropy (<5 times) across likely extrinsic diffusional speeds.

Conclusions

We find that the anisotropy of Mg diffusion in forsterite is heavily dependent upon conditions with pressure strongly decreasing the anisotropy while temperature only weakly affects it. In the presence of extrinsic vacancies temperature strongly controls diffusional anisotropy with samples at low

temperatures having potentially extremely high diffusional anisotropy (>500 times faster in the [001] direction).

In this work we outline a simple atomistic model which is able to replicate measured experimental diffusion rates along the [001] direction. We find that to explain experimental diffusion rates in the [100] and [010] directions interstitial diffusion is required alongside Mg diffusion.

The next step is to consider how other components could affect this diffusion such as has been seen with enstatite (Jollands et al., 2020) and with our simple extrinsic vacancy model in Figure 8. Additional components can either affect the number and balance of Mg vacancies and interstitials or they can affect the intrinsic diffusion of Mg vacancies and interstitials. The former effect can be considered by examining the energetics of defect forming reactions and how contaminants change these energetics- particularly through changing the configurational entropy balances- and the latter can be considered for contaminants that directly change Mg vacancies or interstitials by interacting with them.

Acknowledgments

Funding was provided by the National Environment Research Council as part of the Volatiles, Geodynamics and Solid Earth Controls on the Habitable Planet research programme (NE/M000044/1) and by National Natural Science Foundation of China (41773057). JM is highly thankful to Chinese Academy of Sciences (CAS) for PIFI.

Bibliography

- AMMANN, M. W., BRODHOLT, J. P., WOOKEY, J. & DOBSON, D. P. 2010. First-principles constraints on diffusion in lower-mantle minerals and a weak D'' layer. *Nature*, 465, 462-465.
- ANDERSSON, K. 1987. *Materietransport und Defektstrukturen in kristallinem Magnesiumorthosilicat bei höheren Temperaturen*. Technischen Universität Clausthal.
- ANDERSSON, K., BORCHARDT, G., SCHERRER, S. & WEBER, S. 1989. Self-diffusion in Mg₂SiO₄ (forsterite) at high temperature. *Fresenius Zeitschrift Fur Analytische Chemie*, 333, 383-385.
- BAGATUR'YANTS, A. A., KORKIN, A. A., NOVOSELOV, K. P., SAVCHENKO, L. L. & UMANSKII, S. Y. 2003. Integrated approach to atomistic simulation of film deposition processes. *In: CATLOW, C. R. A. & KOTOMIN, E. A. (eds.) Computational Materials Science*. USA: IOS Press.

- BEJINA, F., BLANCHARD, M., WRIGHT, K. & PRICE, G. D. 2009. A computer simulation study of the effect of pressure on Mg diffusion in forsterite. *Physics of the Earth and Planetary Interiors*, 172, 13-19.
- BORTZ, A. B., KALOS, M. H. & LEBOWITZ, J. L. 1975. NEW ALGORITHM FOR MONTE-CARLO SIMULATION OF ISING SPIN SYSTEMS. *Journal of Computational Physics*, 17, 10-18.
- BRODHOLT, J. 1997. Ab initio calculations on point defects in forsterite (Mg₂SiO₄) and implications for diffusion and creep. *American Mineralogist*, 82, 1049-1053.
- BULATOV, V. V. & CAI, W. 2006. *Computer Simulations of Dislocations*, UK, Oxford University Press.
- CHAKRABORTY, S. 2010. Diffusion Coefficients in Olivine, Wadsleyite and Ringwoodite. In: ZHANG, Y. X. & CHERNIAK, D. J. (eds.) *Diffusion in Minerals and Melts*.
- CHAKRABORTY, S., FARVER, J. R., YUND, R. A. & RUBIE, D. C. 1994. MG TRACER DIFFUSION IN SYNTHETIC FORSTERITE AND SAN-CARLOS OLIVINE AS A FUNCTION OF P, T AND FO₂. *Physics and Chemistry of Minerals*, 21, 489-500.
- CLARK, S. J., SEGALL, M. D., PICKARD, C. J., HASNIP, P. J., PROBERT, M. J., REFSON, K. & PAYNE, M. C. 2005. First principles methods using CASTEP. *Zeitschrift fuer Kristallographie*, 220, 567-570.
- DOHMEN, R., BECKER, H.-W. & CHAKRABORTY, S. 2007. Fe-Mg diffusion in olivine I: experimental determination between 700 and 1,200 degrees C as a function of composition, crystal orientation and oxygen fugacity. *Physics and Chemistry of Minerals*, 34, 389-407.
- DOHMEN, R. & CHAKRABORTY, S. 2007. Fe-Mg diffusion in olivine II: point defect chemistry, change of diffusion mechanisms and a model for calculation of diffusion coefficients in natural olivine. *Physics and Chemistry of Minerals*, 34, 409-430.
- DOWNS, R. T., ZHA, C. S., DUFFY, T. S. & FINGER, L. W. 1996. The equation of state of forsterite to 17.2 GPa and effects of pressure media. *American Mineralogist*, 81, 51-55.
- FEI, H. Z., KOIZUMI, S., SAKAMOTO, N., HASHIGUCHI, M., YURIMOTO, H., MARQUARDT, K., MIYAJIMA, N. & KATSURA, T. 2018. Mg lattice diffusion in iron-free olivine and implications to conductivity anomaly in the oceanic asthenosphere. *Earth and Planetary Science Letters*, 484, 204-212.
- HARTLEY, M. E., MORGAN, D. J., MACLENNAN, J., EDMONDS, M. & THORDARSON, T. 2016. Tracking timescales of short-term precursors to large basaltic fissure eruptions through Fe-Mg diffusion in olivine. *Earth and Planetary Science Letters*, 439, 58-70.
- ISAAK, D. G., ANDERSON, O. L., GOTO, T. & SUZUKI, I. 1989. ELASTICITY OF SINGLE-CRYSTAL FORSTERITE MEASURED TO 1700-K. *Journal of Geophysical Research-Solid Earth and Planets*, 94, 5895-5906.
- JAOUL, O. 1990. MULTICOMPONENT DIFFUSION AND CREEP IN OLIVINE. *Journal of Geophysical Research-Solid Earth and Planets*, 95, 17631-17642.
- JAOUL, O., BERTRANALVAREZ, Y., LIEBERMANN, R. C. & PRICE, G. D. 1995. FE-MG INTERDIFFUSION IN OLIVINE UP TO 9 GPa AT T=600-900-DEGREES-C - EXPERIMENTAL-DATA AND COMPARISON WITH DEFECT CALCULATIONS. *Physics of the Earth and Planetary Interiors*, 89, 199-218.
- JOLLANDS, M. C., ZHUKOVA, I. A., O'NEILL, H. S. & HERMANN, J. 2020. Mg diffusion in forsterite from 1250-1600 °C. *American Mineralogist*, DOI: 10.2138/am-2020-7286.
- KARATO, S., JUNG, H., KATAYAMA, I. & SKEMER, P. 2008. Geodynamic significance of seismic anisotropy of the upper mantle: New insights from laboratory studies. *Annual Review of Earth and Planetary Sciences*.
- LEETMAA, M. & SKORODUMOVA, N. V. 2015. Mean square displacements with error estimates from non-equidistant time-step kinetic Monte Carlo simulations. *Computer Physics Communications*, 191, 119-124.
- LESLIE, M. & GILLAN, M. J. 1985. THE ENERGY AND ELASTIC DIPOLE TENSOR OF DEFECTS IN IONIC-CRYSTALS CALCULATED BY THE SUPERCELL METHOD. *Journal of Physics C-Solid State Physics*, 18, 973-982.
- MORIOKA, M. 1981. CATION DIFFUSION IN OLIVINE .2. NI-MG, MN-MG, MG AND CA. *Geochimica Et Cosmochimica Acta*, 45, 1573-1580.

- OZAWA, K. 1984. OLIVINE-SPINEL GEOSPEEDOMETRY - ANALYSIS OF DIFFUSION-CONTROLLED MG-FE-2+ EXCHANGE. *Geochimica Et Cosmochimica Acta*, 48, 2597-2611.
- PANKHURST, M. J., MORGAN, D. J., THORDARSON, T. & LOUGHLIN, S. C. 2018. Magmatic crystal records in time, space, and process, causatively linked with volcanic unrest. *Earth and Planetary Science Letters*, 493, 231-241.
- PAYNE, M. C., TETER, M. P., ALLAN, D. C., ARIAS, T. A. & JOANNOPOULOS, J. D. 1992. ITERATIVE MINIMIZATION TECHNIQUES FOR ABINITIO TOTAL-ENERGY CALCULATIONS - MOLECULAR-DYNAMICS AND CONJUGATE GRADIENTS. *Reviews of Modern Physics*, 64, 1045-1097.
- POIRIER, J. P. 1985. *Creep in Crystals*, UK, Cambridge University Press.
- SCHOCK, R. N., DUBA, A. G. & SHANKLAND, T. J. 1989. ELECTRICAL-CONDUCTION IN OLIVINE. *Journal of Geophysical Research-Solid Earth and Planets*, 94, 5829-5839.
- TENG, F. Z., DAUPHAS, N., HELZ, R. T., GAO, S. & HUANG, S. C. 2011. Diffusion-driven magnesium and iron isotope fractionation in Hawaiian olivine. *Earth and Planetary Science Letters*, 308, 317-324.
- TILLEY, R. J. D. 1987. *Defect Crystal chemistry and its applications*, United States, Kluwer Academic Publishers.
- VINEYARD, G. H. 1957. FREQUENCY FACTORS AND ISOTOPE EFFECTS IN SOLID STATE RATE PROCESSES. *Journal of Physics and Chemistry of Solids*, 3, 121-127.
- VOCADLO, L., WALL, A., PARKER, S. C. & PRICE, G. D. 1995. ABSOLUTE IONIC-DIFFUSION IN MGO - COMPUTER CALCULATIONS VIA LATTICE-DYNAMICS. *Physics of the Earth and Planetary Interiors*, 88, 193-210.
- VOTER, A. F. 2007. INTRODUCTION TO THE KINETIC MONTE CARLO METHOD. In: SICKAFUS, K. E., KOTOMIN, E. A. & UBERUAGA, B. P. (eds.) *Radiation Effects in Solids*. Dordrecht: Springer.
- WALKER, A. M., WOODLEY, S. M., SLATER, B. & WRIGHT, K. 2009. A computational study of magnesium point defects and diffusion in forsterite. *Physics of the Earth and Planetary Interiors*, 172, 20-27.
- WEAST, R. C. A., M. J. 1981. *CRC Handbook of Chemistry and Physics*, Boca Raton, CRC Press.
- WRIGHT, K. & CATLOW, C. R. A. 1994. A computer simulation study of (OH) defects in olivine. *Physics and Chemistry of Minerals*, 20, 515-518.
- YOSHINO, T., MATSUZAKI, T., SHATSKIY, A. & KATSURA, T. 2009. The effect of water on the electrical conductivity of olivine aggregates and its implications for the electrical structure of the upper mantle. *Earth and Planetary Science Letters*, 288, 291-300.
- YOSHINO, T., ZHANG, B. H., RHYMER, B., ZHAO, C. C. & FEI, H. Z. 2017. Pressure dependence of electrical conductivity in forsterite. *Journal of Geophysical Research-Solid Earth*, 122, 158-171.
- ZHANG, Z., STIXRUDE, L. & BRODHOLT, J. 2013. Elastic properties of MgSiO₃-perovskite under lower mantle conditions and the composition of the deep Earth. *Earth and Planetary Science Letters*, 379, 1-12.

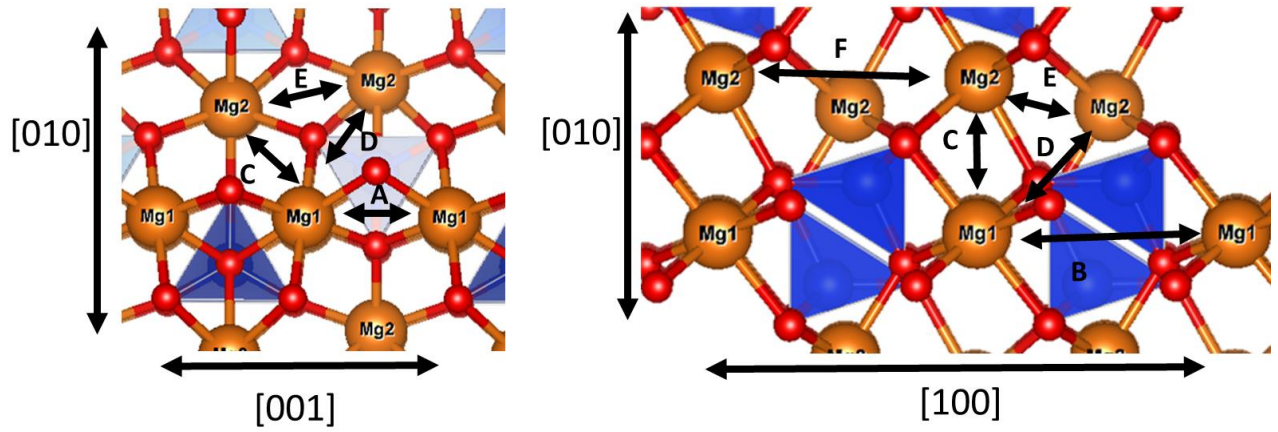


Figure 1:

Diagram of possible vacancy hops between M1 and M2 sites. The absolute distances of these hops are listed in Table S4. Mg atoms are brown, Si atoms are blue with their tetrahedrons highlighted, oxygen atoms are red.

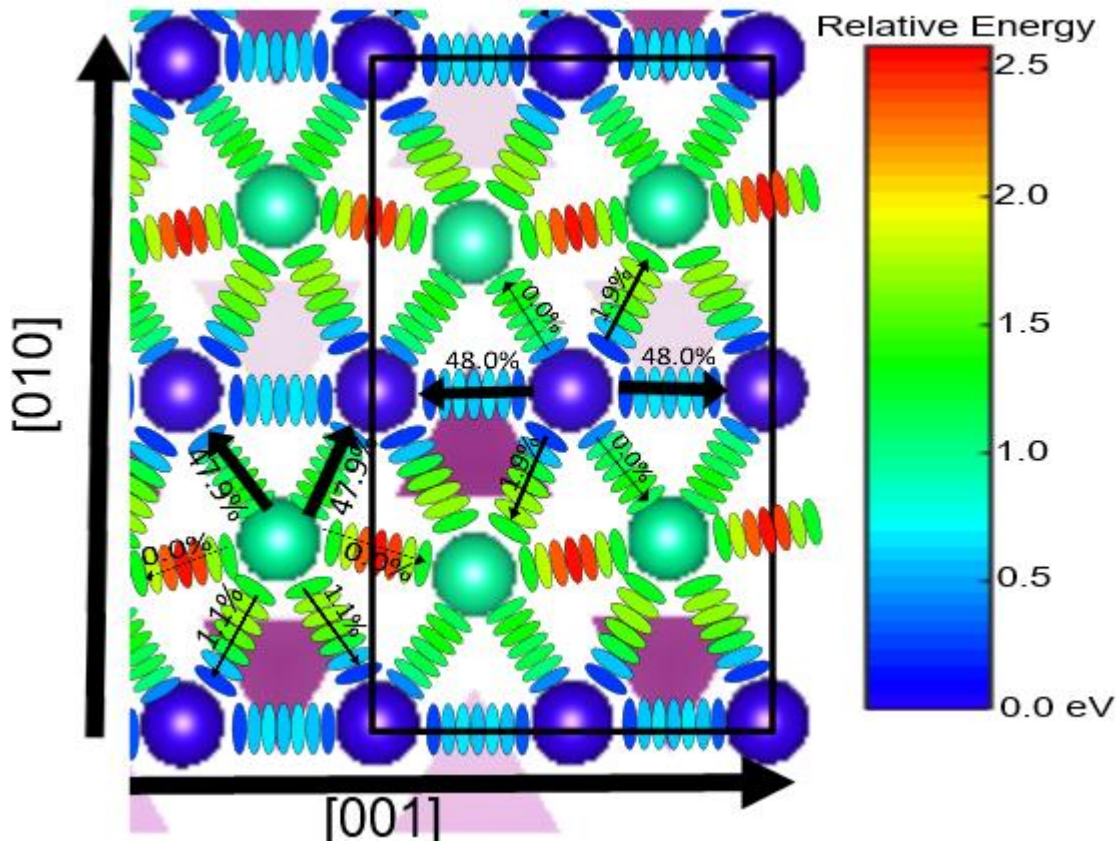


Figure 2: Plot of the activation energy barriers to Mg vacancy hopping in anhydrous forsterite. The energy of a vacancy is plotted at M1 (blue) (defined as 0 eV) and M2 (green) sites and at 7 points in-between each site with both the site and the intermediate points plotted with the same relative energy bar as shown. Many more intermediate points were used to determine the activation energy maximum (see text for details). Hops in the [100] direction (hops B and F) are not shown but both of these hops have activation energies higher than all the hops pictured here. The black box represents a forsterite unit cell. For a sample M1 and an M2 site we have shown the main hops with a percentage likelihood of selecting this hop that was determined at 1300 K and 0 GPa (uncorrected).

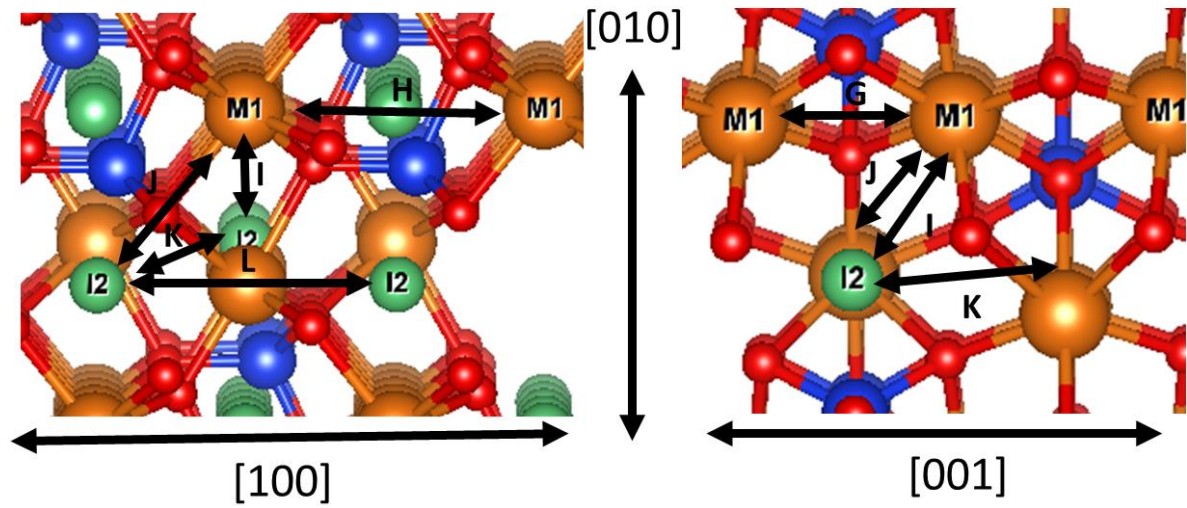


Figure 3:

Diagram of interstitial hops between M1 and I2 sites. The absolute distances of these hops are listed in Table S8. Octahedral holes are green.

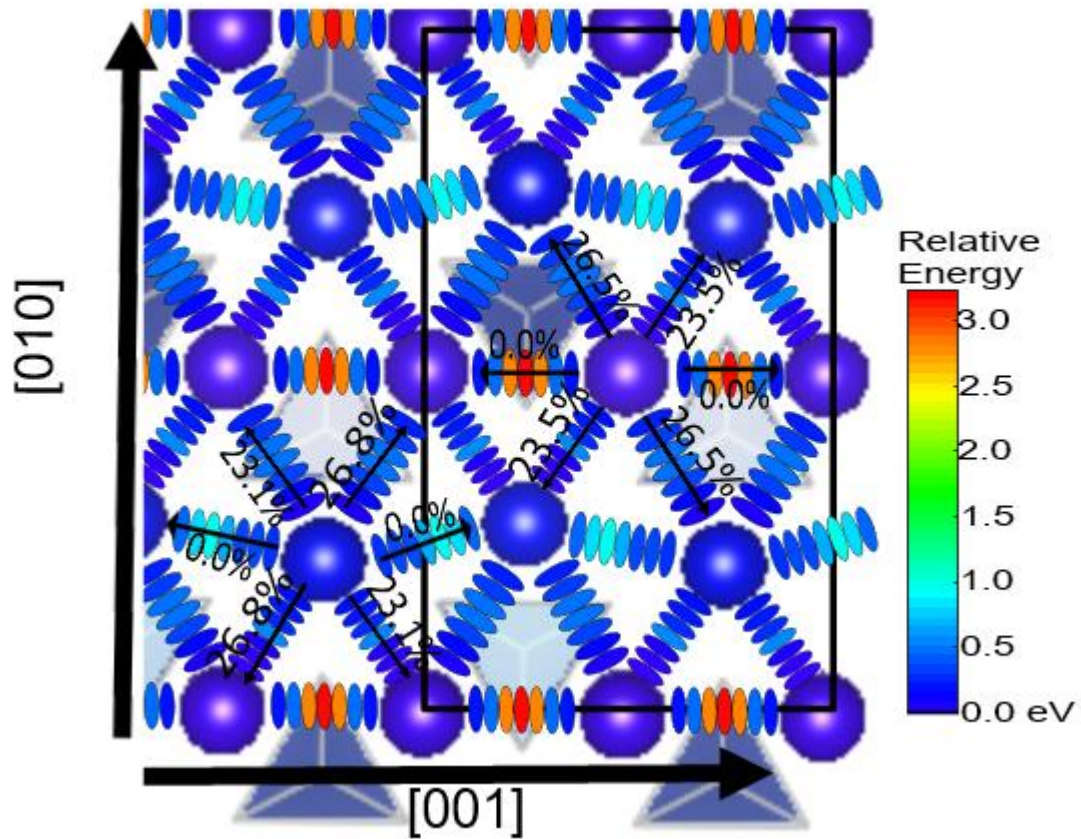


Figure 4: As Figure 2 but for interstitial hops between M1 and I2 sites with the M1 sites being defined as 0 eV. The layer closer to the bottom of the graph are M1 and then I2 and M1 layers alternate going up the page. These sites are much closer in energy than the M1 and M2 sites for vacancy migration. Again hops along the [100] axis (H and L) are not shown but are very high in energy. With this projection I and I* and J and J* hops are on top of each other (as they are only varied along the [100] direction) but we have pictured the lower energy paths (I and J respectively).

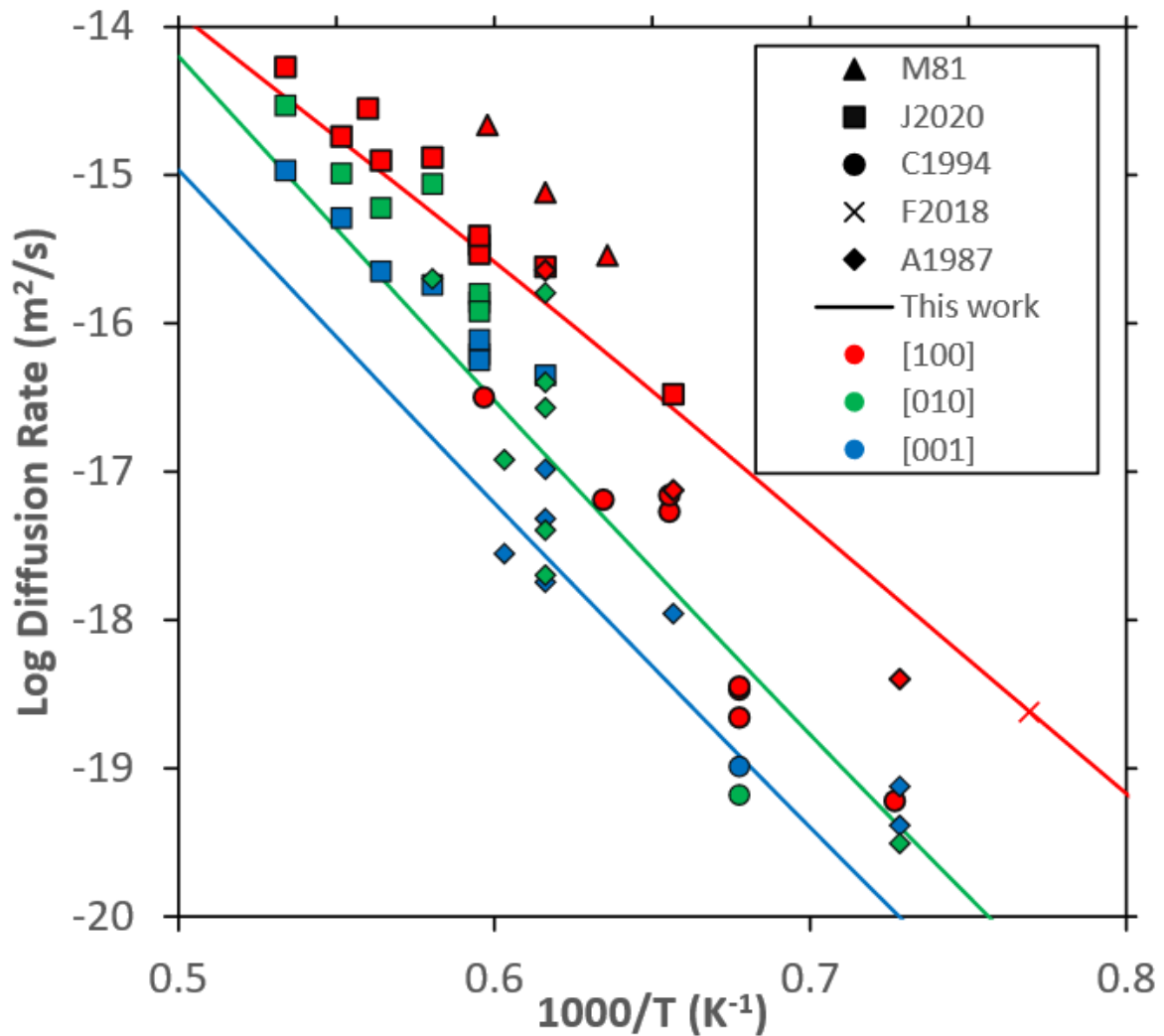


Fig 5: Plot of experimental Mg self diffusion rates in MgO-buffered forsterite at 0 GPa alongside our predicted rates at 0 GPa (corrected) determined by fitting between our pressure corrected values (the same plot with a 5 GPa pressure correction is shown in Fig S4). Rates have been separated by diffusion direction (colour- red= [001], green= [010], blue= [100]) and by the work they come from (symbol-see below). The lines represent our own calculations. In this collection we have excluded work in olivine and work buffered by enstatite. The mark for Fei *et al.* (2018a) was determined by our own extrapolation of the high temperature data across different pressures, all other points were as measured in the experiment. References are Morioka *et al.* 1981 triangles, Jollands *et al.* 2020 squares, Chakraborty *et al.* 1994 circles, Fei *et al.* (2018a) cross, Andersson *et al.* 1987 diamonds.

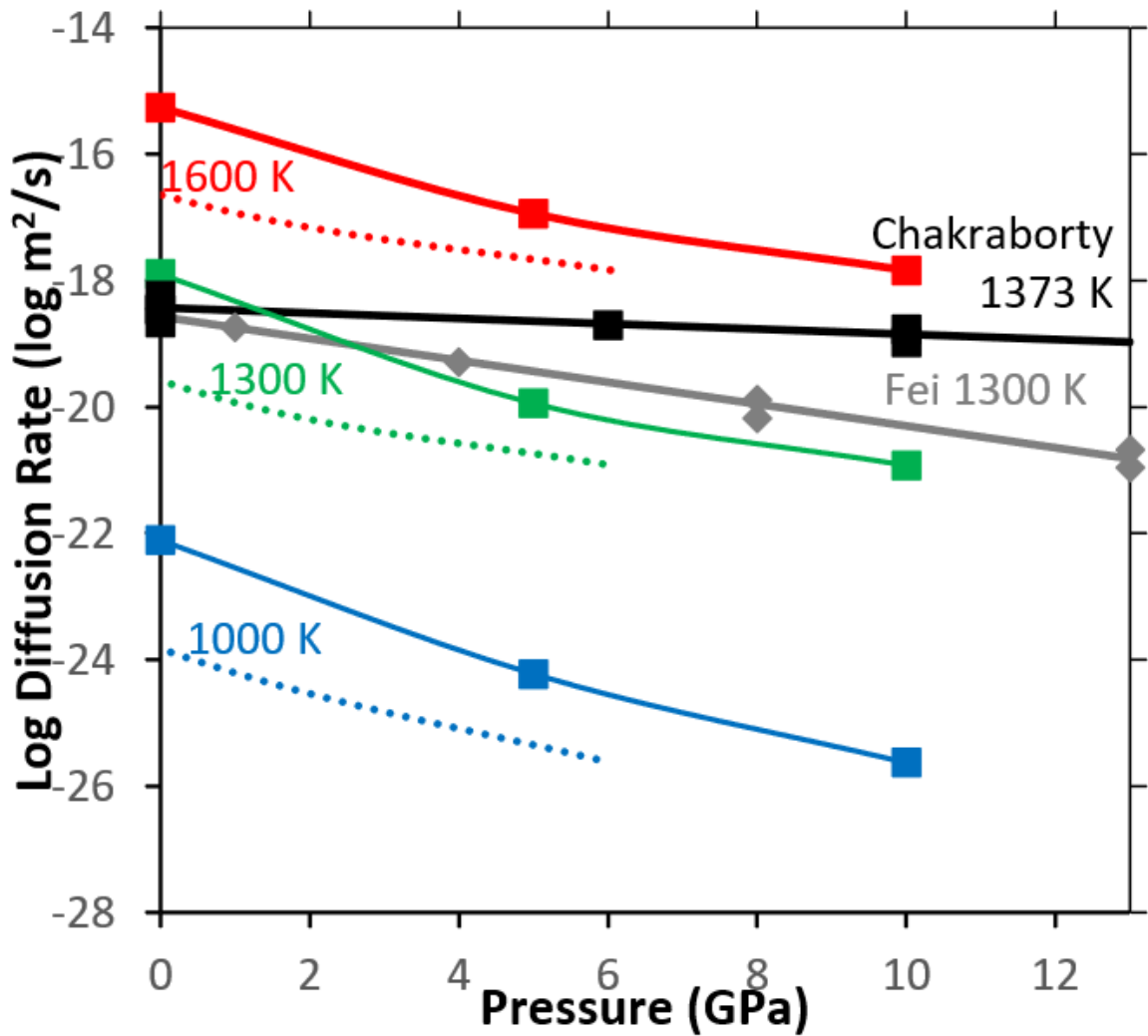


Figure 6: [001] Mg diffusion rates in perfect forsterite as a function of pressure at fixed temperatures (blue=1000 K, green=1300 K, red=1600 K) compared to results from Chakraborty *et al.* (1994) and Fei *et al.* (2018a). Model predictions are uncorrected (solid line) or pressure corrected (dotted line). For experimental data data points are plotted and then a line is constructed using activation volumes of 1.1 cm³/mol for Fei *et al.* (1994) and 4.3 cm³/mol for Fei *et al.* (2018a). The results from Chakraborty *et al.* (1994) are those with no buffer with an f_{O_2} of 10^{-12} . In these results a higher activation volume (~ 3.4) was determined in air. The oxygen fugacity of Fei *et al.* (2018a) is unknown due to the complicated presence of water.

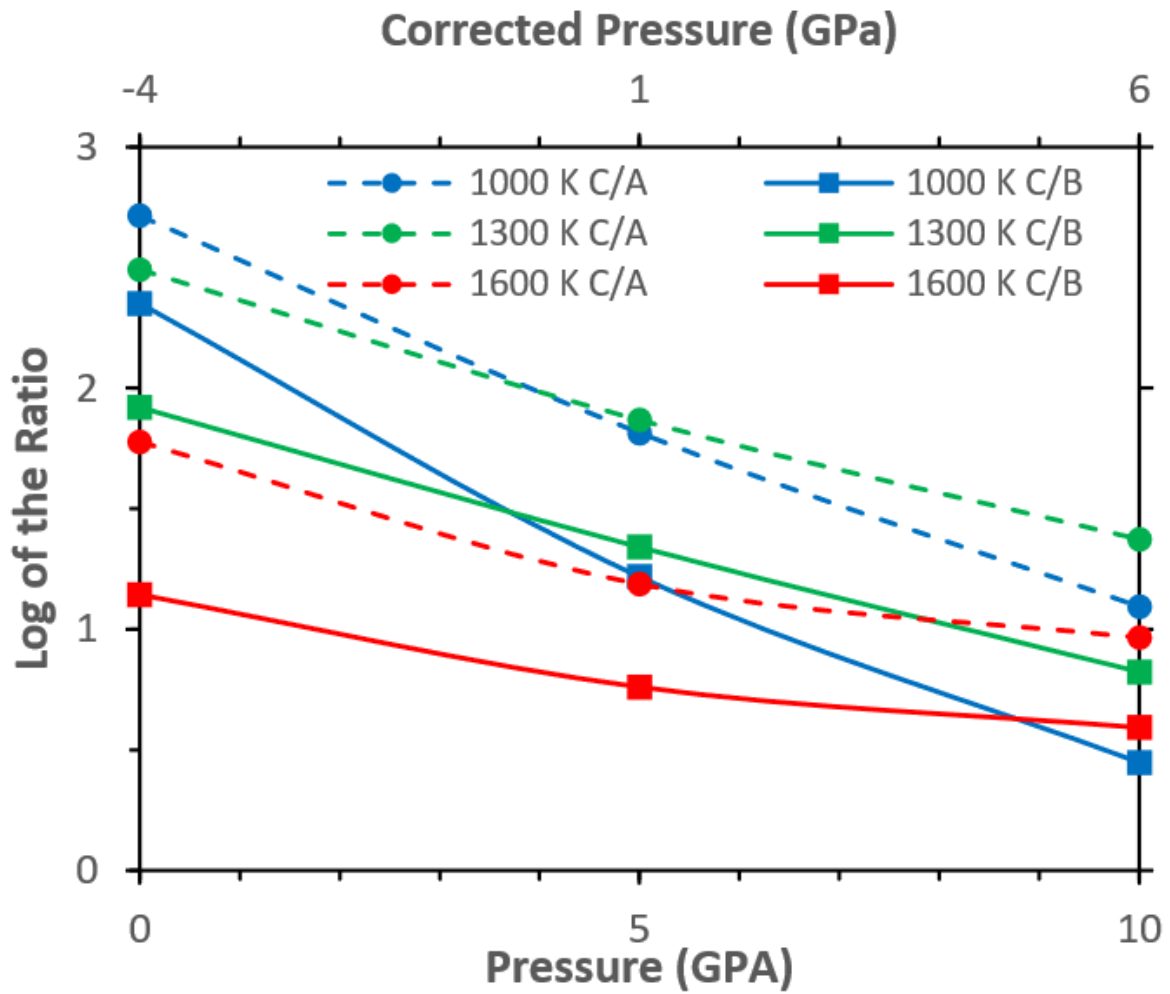


Figure 7: Log of the ratios of C/A ([001]/[100]) (dotted lines, circles) and C/B ([001]/[010]) Mg diffusion (solid line, squares) in perfect olivine as a function of pressure at different temperatures (blue 1000 K, green 1300, red 1600). Two pressure scales are shown, the pressure scale from DFT and one that has been corrected as per the text.

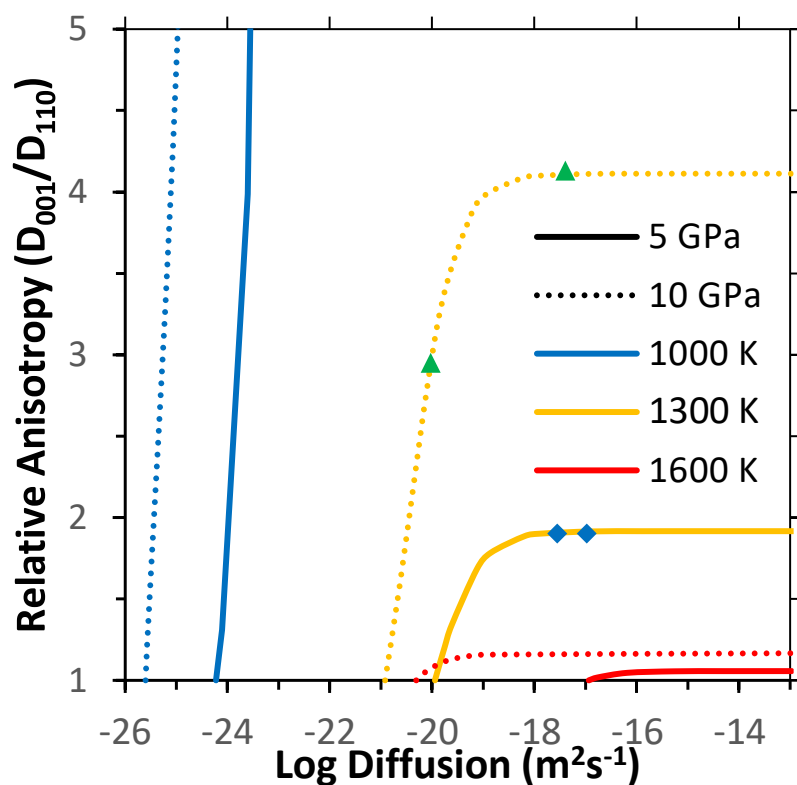


Fig 8 Comparison of anisotropy (defined as diffusion in the [001] direction/ diffusion in the [110] direction) for different diffusion rates where we assume that diffusion rates were increased via external Mg vacancies. Lines are at 1000 (blue), 1300 (orange) and 1600 K and solid lines represent 5 GPa, dotted lines 10 GPa (uncorrected) which correct to around 1 and 6 GPa respectively. This graph was constructed by assuming that Mg vacancy mobility remained fixed to its intrinsic value and then adding in extra vacancies to the intrinsic defect concentration until the desired diffusion rate was met.

The blue diamonds represent the range of diffusion between Fe=1-20% for olivine at 0 GPa, 1300 K and $fO^2=10^{-7}$ Dohmen and Chakraborty (2017). The green triangle represents the range of diffusion for water ranging between 1-150 wt. ppm at ~8 GPa and 1300 K (Fei *et al.* 2018). These values are to show how anisotropy would vary across the range of two common defects.

| | 0 GPa | 5 | 10 |
|------|------------------------|------------------------|------------------------|
| | Formation Energy (eV) | | |
| 0 K | 5.65 | 6.43 | 6.54 |
| 1000 | 4.94 | 5.96 | 6.37 |
| 1300 | 4.73 | 5.78 | 6.27 |
| 1600 | 4.52 | 5.60 | 6.13 |
| | Vacancy Concentration | | |
| 1000 | 4.13×10^{-13} | 3.06×10^{-15} | 9.23×10^{-17} |
| 1300 | 8.51×10^{-10} | 8.81×10^{-12} | 9.37×10^{-13} |
| 1600 | 9.59×10^{-08} | 2.14×10^{-09} | 2.89×10^{-10} |

Table 1: Free energy of the Frenkel reaction at various pressures and temperatures and the corresponding concentration of vacancies and interstitials (in defects/unit cell) in a pure forsterite crystal where only the Mg Frenkel reaction forms significant defects- this concentration is for each defect type so the concentration of total defects (vacancies+interstitials) is twice this number. Also shown is the concentration of hydrous vacancies formed by water assuming water solely forms hydrous Mg vacancies ($\gamma=1$). All pressures are uncorrected.

| | | Anhydrous Vacancy | | Anhydrous Interstitial | |
|----------------------|-------------|---------------------|-------------------------|------------------------|-------------------------|
| | | E _a (eV) | v (Hz) | E _a (eV) | v (Hz) |
| Hops from M1 Site | | | | | |
| A/G | M1-M1 | 0.75 | 1.01 x 10 ¹³ | 3.22 | 9.11 x 10 ⁰⁸ |
| B/H | M1-M1 | 4.12 | 3.71 x 10 ¹⁵ | 3.16 | 1.22 x 10 ¹⁰ |
| C/I | M1-M2/I2 | 1.45 | 2.37 x 10 ¹⁴ | 0.59 | 3.01 x 10 ⁰⁹ |
| I* | M1-I2 | | | 1.35 | 2.38 x 10 ⁰⁸ |
| D/J | M1-M2/I2 | 1.91 | 4.39 x 10 ¹⁴ | 0.56 | 2.02 x 10 ⁰⁹ |
| D*/J* | M1-M2/I2 | 1.91 | 4.39 x 10 ¹⁴ | 1.29 | 2.80 x 10 ⁰⁹ |
| Hops From M2/I2 Site | | | | | |
| C/I | M2/I2-M1 | 0.45 | 1.15 x 10 ¹⁴ | 0.39 | 1.41 x 10 ¹³ |
| I* | M1-I2 | | | 1.15 | 1.11 x 10 ¹² |
| D/J | M2/I2-M1 | 1.00 | 2.13 x 10 ¹⁴ | 0.36 | 9.46 x 10 ¹² |
| D*/J* | M2/I2-M1 | 1.00 | 2.13 x 10 ¹⁴ | 1.09 | 1.31 x 10 ¹³ |
| E/K | M2/I2-M2/I2 | 1.65 | 4.27 x 10 ¹⁴ | 1.08 | 5.53 x 10 ¹² |
| F/L | M2/I2-M2/I2 | 2.82 | 2.31 x 10 ¹⁵ | N/A | N/A |

Table 2: Activation energy and attempt frequency of various hops (shown in Figure 1 and 3 with the hop distances outlined in Table S4 and S8) for hydrous and anhydrous forsterite at 0 GPa uncorrected. Hop L could not be stabilised but is very high in energy. Hops with an asterisk go in the reverse direction where this is not equivalent.

| | | [100] | [010] | [001] | [001] 5 GPa | [001] 10 GPa |
|----------------------|--------|------------------------|------------------------|------------------------|------------------------|------------------------|
| Anhydrous vacancy | 1000 K | 1.58×10^{-14} | 6.61×10^{-14} | 1.91×10^{-10} | 1.88×10^{-10} | 1.88×10^{-10} |
| | 1300 | 3.37×10^{-12} | 1.42×10^{-11} | 1.48×10^{-09} | 1.27×10^{-09} | 1.19×10^{-09} |
| | 1600 | 9.15×10^{-11} | 4.02×10^{-10} | 5.71×10^{-09} | 5.30×10^{-09} | 4.93×10^{-09} |
| Interstitial | 1000 | 3.47×10^{-13} | 7.58×10^{-13} | 2.65×10^{-13} | 6.13×10^{-12} | 6.66×10^{-11} |
| | 1300 | 1.39×10^{-12} | 3.62×10^{-12} | 1.18×10^{-12} | 1.39×10^{-11} | 8.44×10^{-11} |
| | 1600 | 3.83×10^{-12} | 7.86×10^{-12} | 3.96×10^{-12} | 2.46×10^{-11} | 1.01×10^{-10} |

Table 3: Diffusion coefficients (m^2/s) of vacancies and interstitials in three directions at 0 GPa (uncorrected) with 5 and 10 GPa (uncorrected) [001] diffusion coefficients also listed. For the other coefficients in [100] and [010] at 5 and 10 GPa see Table S10 and S11.

Supplementary Methods

In this paper we calculate diffusion of Mg in forsterite through a 3 step process. In the first step we calculate the activation energy and frequency of various hops. In the second step we put these hopping results into a Kinetic-Monte Carlo algorithm (KMC). In the third step we combine the results of the KMC with a calculation of defect concentrations also calculated with DFT.

Each of these steps has additional information provided here. To validate our results in the first step and compare with previous work we also calculated the activation energies with forcefield calculations and the parameters of these calculations are outlined below. In the second step we use a KMC algorithm which is described briefly in the paper but is described fully below. In the third step we calculate defect concentrations by minimising the free energy. To do this we need to know the free energy of different concentrations of defects and the equations to calculate this are provided below.

Forcefield Calculations:

To compare our answers with earlier work we calculated hop energies using forcefield calculations. These calculations were done with GULP (Gale, 1997) and a forcefield designed for wet olivine (Wright and Catlow, 1994, Lewis and Catlow, 1985, Schroder et al., 1992). The parameters of this are given in Table S13. This potential reproduces the physical properties of forsterite reasonably well (Price et al., 1987) and has previously been used to model forsterite point defects as for example in Bejina et al. (2009) and Walker et al. (2009).

This potential models cations with a formal charge (Mg 2+, Si 4+) whereas O atoms are modelled as a positively charged core (+0.84819) with a negatively charged massless shell (-2.84819). All cation-anion pairs are joined by a Buckingham potential and SiO₄ tetrahedra are fixed with a harmonic three body potential. H⁺ ions in this potential are represented by O-H groups using a Morse potential where the participating oxygen ion is represented by a partially ionic point charge. To place the hydrogen we used the most stable arrangements of hydrogen that were determined by DFT- in M1 vacancies both H are bound to an O2 atom, in M2 vacancies one is bound to an O1 and one to an O3 atom.

Columbic energy was calculated using the Wolf sum (Wolf et al., 1999) which uses a charge neutralizing term to guarantee convergence of the energy at a finite distance. Its cutoff was set to

15 Å with a damping parameter $\alpha=0.2 \text{ \AA}^{-1}$. For charged systems a neutralising uniform charged background was added.

We used the same unit cells (2x2x1) as for DFT cells and also a cell that was twice as large (4x4x2). Doubling the cell size changed the activation of the hops by $<0.1 \text{ eV}$.

Two methods were used to find the transition state of the hops. Firstly we used the constrained optimisation method that is outlined in the methods for DFT calculations. Then we took the resulting optimisation state and used the RFO optimisation routine in GULP to find the nearest stationary point with 1 negative frequency. This second step changed our activations by less than 10 meV which shows that our constrained optimisation method produces transition states that are reasonably accurate.

Kinetic Monte Carlo Algorithm

In this section we shall describe our KMC algorithm while a flow diagram presenting the same information is shown in Figure S5. For each state (e.g. a vacancy on M1 or a vacancy on M2) we evaluate the rate of each of the k^i hops escaping from that state (equation 8 using equations 9), sum these to give k^{tot} and calculate the probability of each hop from $p^i = \frac{k^i}{k^{\text{tot}}}$. This provides a “transition matrix”, which encodes the probability of each transition from a given starting state to each reachable final state. Symmetrically equivalent hops in different directions are included separately in this matrix. We separately store the jump vectors for each transition in the matrix, “unwrapping” the periodicity of the crystal. Our algorithm is initialised by choosing an initial state, a start time, and position for the defect. We then proceed as follows:

- 1) Draw two uniform random numbers (r^1 and r^2) from the interval [0,1].
- 2) Using r^1 select a hop out of the current state based on weighted probabilities p^i by placing the probabilities of each hop (p^i) end to end in a line from 0 to 1 and then selecting the hop that occurs at r^1 along the line (see Fig S2 and Fig S3).
- 3) Using r^2 determine the time spent in the state:
$$t^i = -\left(\frac{1}{k^{\text{tot}}}\right) \ln(r^2) \text{ Equation S1}$$
- 4) Update the state index and defect position using the selected hop, advance time by t^i
- 5) Return to 1

As this algorithm progresses, we build a list of positions of the defect as a function of time as it undergoes a random walk through the (infinite) crystal structure. This is the information we need to calculate the diffusion coefficient from the mean squared displacement (MSD).

Calculating the MSD with non-equidistant time steps is not straightforward and doing this with error propagation particularly cumbersome. A rigorous method of MSD and error calculation for non-equidistant timesteps has been presented by Leetmaa and Skorodumova (2015) and has been used in this work. After every hop (step 4) we compare the current position of the particle and the time with the particle positions and the time for the previous N simulation steps where N is referred to as the history window. For each comparison the squared displacement is calculated and these are then binned by the difference in time into a histogram D(t) with the number of squared displacements in each bin recorded as a separate histogram H(t). Mean squared displacement for each bin (ρ_i) is then:

$$\rho_i = D_i/H_i \text{ Equation S2}$$

which is then plotted against time (see for example Figure S6) with the time of each bin taken as the centre of that bins time window. The MSD $\langle x^2 \rangle$ trace is related to diffusion by:

$$\langle x^2 \rangle = q_i D t \text{ Equation S3}$$

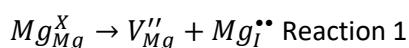
so that the diffusion coefficient D can be found by calculating the slope of $\langle x^2 \rangle$ against $q_i t$. In all of our calculations the total number of runs (M) was 50,000,000, the history window (N) was 50,000, 200,000 bins were used to bin across a time that varied depending upon the simulation. In this formulation N controls the total length of diffusion whereas M controls the accuracy/number of samplings. Standard deviation of our data was calculated using the method in Leetmaa and Skorodumova (2015) using the infinite limit for $n_e(t)$ as our N values are large.

As a test of this method we calculated the diffusion rate of Mg diffusion in MgO. This was determined analytically in Vocadlo *et al.* (1995) and our KMC method produced diffusion rates that were within 1% of the analytical values ($1.76 \cdot 10^{-27}$ vs $1.78 \cdot 10^{-27}$ m/s²) even with quite low MSD parameter cutoffs (M=2,000,000, N=20,000)

Finding the equilibrium concentration of defects:

To calculate diffusion we need to know the concentration of defects in our system.

We assume the Mg Frenkel reaction (Reaction 1) is the primary source of intrinsic Mg defects in forsterite:



We can calculate the equilibrium concentration of defects by calculating the free energy minimum of this reaction.

This is not entirely straightforward due to the fact that Mg interstitials can easily occupy two different sites (M1 and I2) with little energy difference between them (Table S2). We thus need to use a Gibb's entropy calculation to work out the probability of Mg interstitials occupying the different sites and the configuration entropy that results.

This is done as follow. We first calculate the reaction energy (ΔE) of R1 which is the enthalpy and vibrational energy change of proceeding Reaction 1 to the right. We define a reaction vector (a) which is between 0 and 1 and which determines how far R1 proceeds to the right with 0 being the production of no defects and 1 being the production of entirely defects. This x also defines the concentration of vacancies and interstitials that are produced.

Free energy as a function of a is then determined using the following equation:

$$\Delta G = \Delta E \times a - TS_{confa} \text{ Equation S4}$$

Where S_{confa} is the configurational entropy at a . This configurational entropy term is determined in the following way. We have 2 defects (vacancy and interstitial) which can each occupy two sites: M1 and M2 for vacancies, M1 and I2 for interstitials. We thus define 4 configurations (i) where the defects of each type are confined to a respective vacancy {Vacancy on M1/Interstitial on M1, M1/I2, M2/M1, M2/I2}. The internal energy of each configuration (U_i) was then calculated using Table S2 with the assumption that temperature does not affect the relative energy of placing defects on different sites. We must then calculate the degeneracy of each configuration (W) which is done using:

$$W = \ln \frac{N!}{a!b!...z!} \text{ Equation S5}$$

Where N is the total number of sites, and a, b, c, \dots, z are the different types of atoms/defects at each site including a final z term, which is simply $(N - a - b - \dots - y)$. To solve this numerically, all defect concentrations were written in terms of defects/mol and then the Stirling approximation was used ($\ln n! \cong n \ln n - n$), giving:

$$W = N \ln N - N - a \ln a + a - b \ln b + b \dots - z \ln z + z \text{ Equation X}$$

To calculate the configurational entropy we then need to know the probability and entropy of each of these configurations. We calculate this using the Gibbs entropy formula:

$$S_{confa} = -k_B \sum_j p_j \ln p_j \text{ Equation S6}$$

Where k_B is the Boltzmann constant. j in Equation S6 represents a specific configuration (i) but in j each configuration appears an equal number of times to its degeneracy (w). p_j represents the probability that each j configuration occurs. The probability of any specific configuration occurring is:

$$p_j = \frac{1}{Z} e^{(-U_j/k_B T)} \text{ Equation S7}$$

Where Z is the canonical partition function

$$Z = \sum_j e^{(-U_j/k_B T)} \text{Equation S8}$$

Equation S6 can then be calculated and this energy added into Equation S4. The reaction vector a in Equation S4 can then be varied until a free energy minimum is found. This then tells us how far forward R1 proceeds at equilibrium and thus the concentration of defects at equilibrium.

Supplementary Results

In our work we simulate diffusion through a series of atomistic hops. These hops are pictured in the text but both vacancy and interstitial hops shall be described below. In our work we also found that water has an effect on activation energy of various vacancy hops. This does not have a large effect on our results as this change is much smaller than the changes in concentration and attempt frequency in a hydrous system but we shall discuss possible reasons for it below.

DIFFERENT SPECIES AND REACTIONS

Vacancy Hops:

The vacancy hops that we study in this work are an A hop (F in Walker *et al.* 2009) between two M1 sites along the [001] direction, a B (A) hop between two M1 sites along the [100] direction through an I1 site, a C (D) and D (E) hop between M1 and M2 sites along the [011] and [111] directions respectively, an E (C) hop between two M2 sites along the [101] direction and an F (B) hop between two M2 sites along the [100] direction through an I2 site. Of the hops that we ruled out there are two important ones. First a direct [001] hop between two M2 sites (analogous to the A hop on the M1 sites) was found to have an activation energy of 4.65 eV, much higher than two E hops which will achieve the same outcome. Second a direct [101] hop between two M1 sites- analogous to the E hop on the M2 sites was found to have a very high activation energy of >7.8 eV due to the presence of both Si and M2 atoms along any possible route.

Interstitial Hops:

The interstitial hops that were studied are a G hop between two M1 sites along [001], a H hop between two M1 sites along [100] through an I1 site, hops I and J between the M1 and I2 sites along

[011] and [111], respectively, a K hop between two I2 sites along [101] and a L hop between two I2 sites along [100] through an M2 site.

Supplementary Information Bibliography

- BEJINA, F., BLANCHARD, M., WRIGHT, K. & PRICE, G. D. 2009. A computer simulation study of the effect of pressure on Mg diffusion in forsterite. *Physics of the Earth and Planetary Interiors*, 172, 13-19.
- DOWNS, R. T., ZHA, C. S., DUFFY, T. S. & FINGER, L. W. 1996. The equation of state of forsterite to 17.2 GPa and effects of pressure media. *American Mineralogist*, 81, 51-55.
- GALE, J. D. 1997. GULP - a computer program for the symmetry adapted simulation of solids. *JCS Faraday Trans*, 93, 629-637.
- LEETMAA, M. & SKORODUMOVA, N. V. 2015. Mean square displacements with error estimates from non-equidistant time-step kinetic Monte Carlo simulations. *Computer Physics Communications*, 191, 119-124.
- LEWIS, G. V. & CATLOW, C. R. A. 1985. POTENTIAL MODELS FOR IONIC OXIDES. *Journal of Physics C-Solid State Physics*, 18, 1149-1161.
- PRICE, G. D., PARKER, S. C. & LESLIE, M. 1987. THE LATTICE-DYNAMICS OF FORSTERITE. *Mineralogical Magazine*, 51, 157-170.
- SCHRODER, K. P., SAUER, J., LESLIE, M., CATLOW, C. R. A. & THOMAS, J. M. 1992. BRIDGING HYDROXYL-GROUPS IN ZEOLITIC CATALYSTS - A COMPUTER-SIMULATION OF THEIR STRUCTURE, VIBRATIONAL PROPERTIES AND ACIDITY IN PROTONATED FAUJASITES (H-Y ZEOLITES). *Chemical Physics Letters*, 188, 320-325.
- WALKER, A. M., WOODLEY, S. M., SLATER, B. & WRIGHT, K. 2009. A computational study of magnesium point defects and diffusion in forsterite. *Physics of the Earth and Planetary Interiors*, 172, 20-27.
- WOLF, D., KEBLINSKI, P., PHILLPOT, S. R. & EGGBRECHT, J. 1999. Exact method for the simulation of Coulombic systems by spherically truncated, pairwise r^{-1} summation. *Journal of Chemical Physics*, 110, 8254-8282.
- WRIGHT, K. & CATLOW, C. R. A. 1994. A computer simulation study of (OH) defects in olivine. *Physics and Chemistry of Minerals*, 20, 515-518.

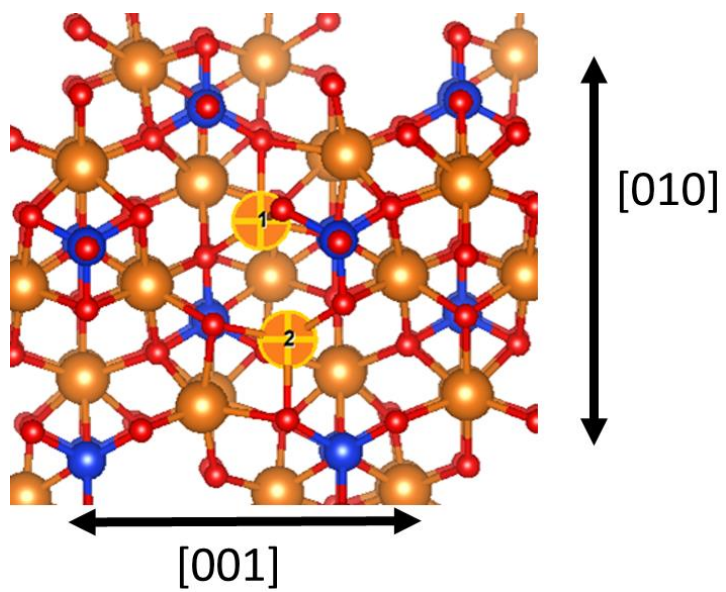
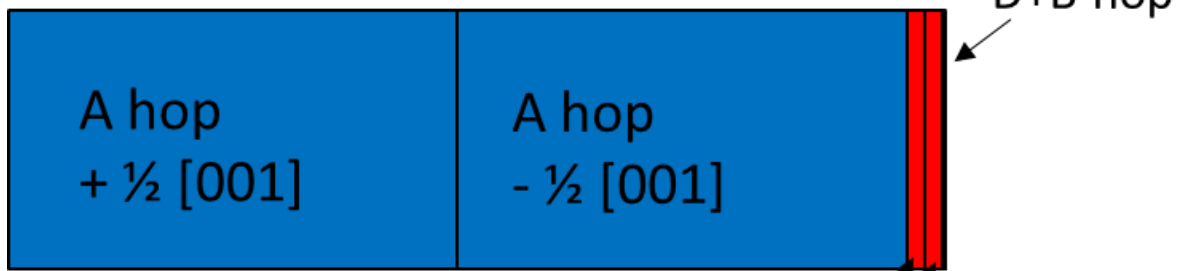


Figure S1: Diagram of the split interstitial Mg arrangement with the two Mg that split across the M1 site highlighted.

Vacancy hops from M1



Vacancy hops from M2

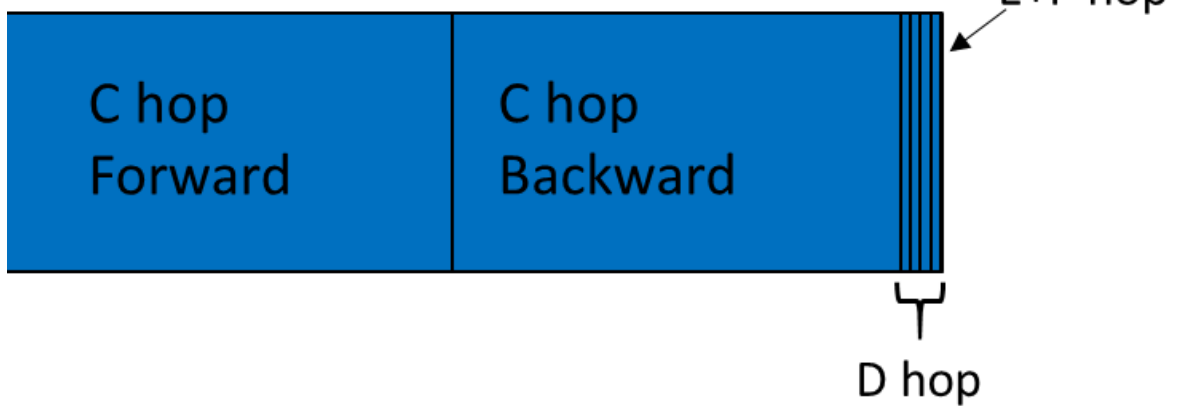


Figure S2: Plot of the different vacancy hops from an M1 and M2 site weighted by the probability of undergoing that hop (determined at 0 GPa and 1300 K). Hops coloured in blue end up in an M1 site, hops coloured in red end up in an M2 site.

Interstitial hops from M1

I*, J*, G+H hop



Interstitial hops from I2

I*, J*, K+L hop



Fig S3: As Figure S2 but for interstitial hops. Hops coloured blue end up on an M1 site, red an I2 site.

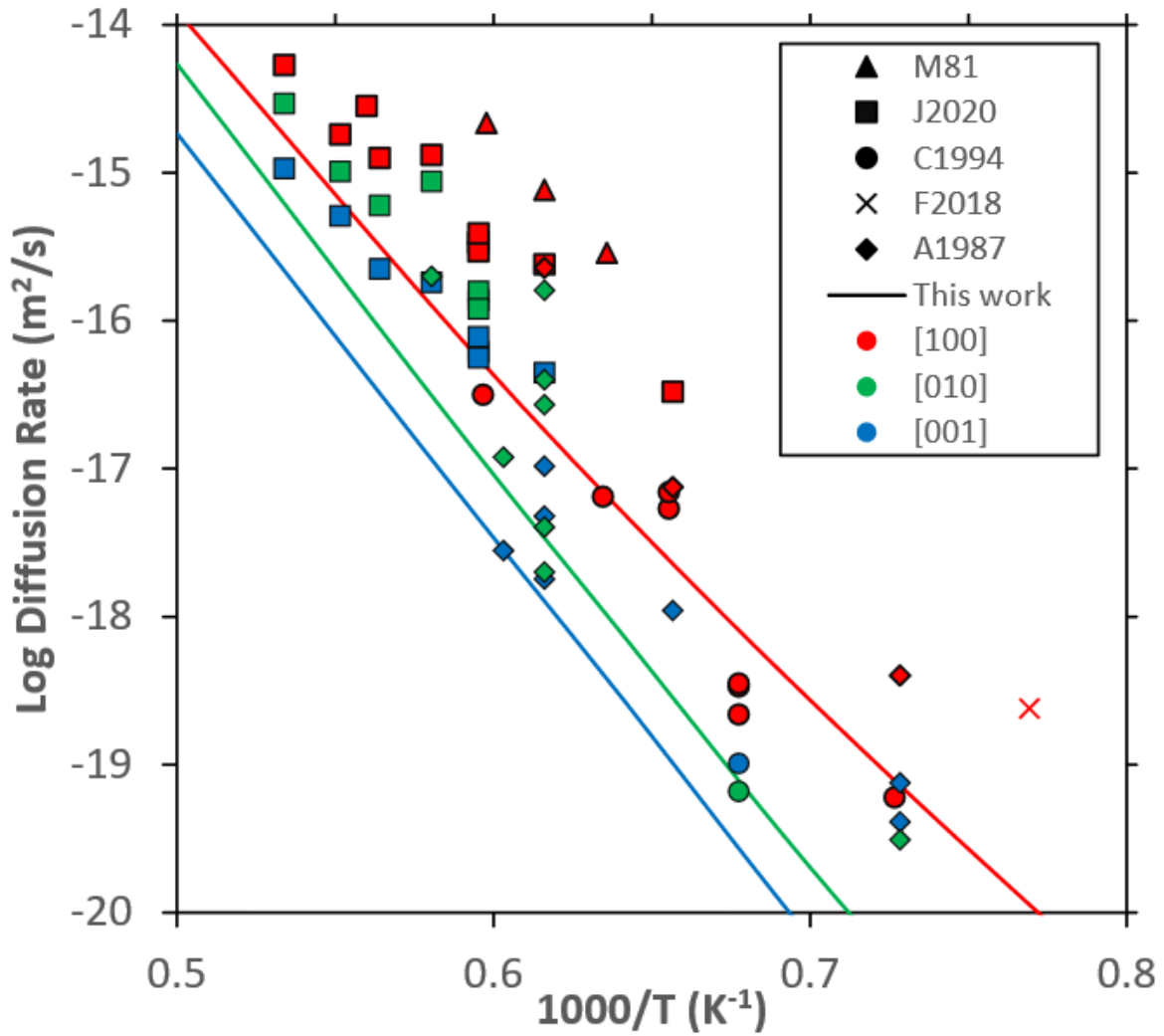


Figure S4: Plot of experimental Mg self diffusion rates in MgO-buffered forsterite at 0 GPa alongside our predicted rates at 0 GPa determined by applying a flat pressure correction of 5 GPa. Rates have been separated by diffusion direction (colour- red= [001], green= [010], blue= [100]) and by the work they come from (symbol-see below). The lines represent our own calculations. In this collection we have excluded work in olivine and work buffered by enstatite. The mark for Fei *et al.* (2018a) was determined by our own extrapolation of the high temperature data across different pressures, all other points were as measured in the experiment. References are Morioka *et al.* 1981 triangles, Jollands *et al.* 2020 squares, Chakraborty *et al.* 1994 circles, Fei *et al.* (2018a) cross, Andersson *et al.* 1987 diamonds.

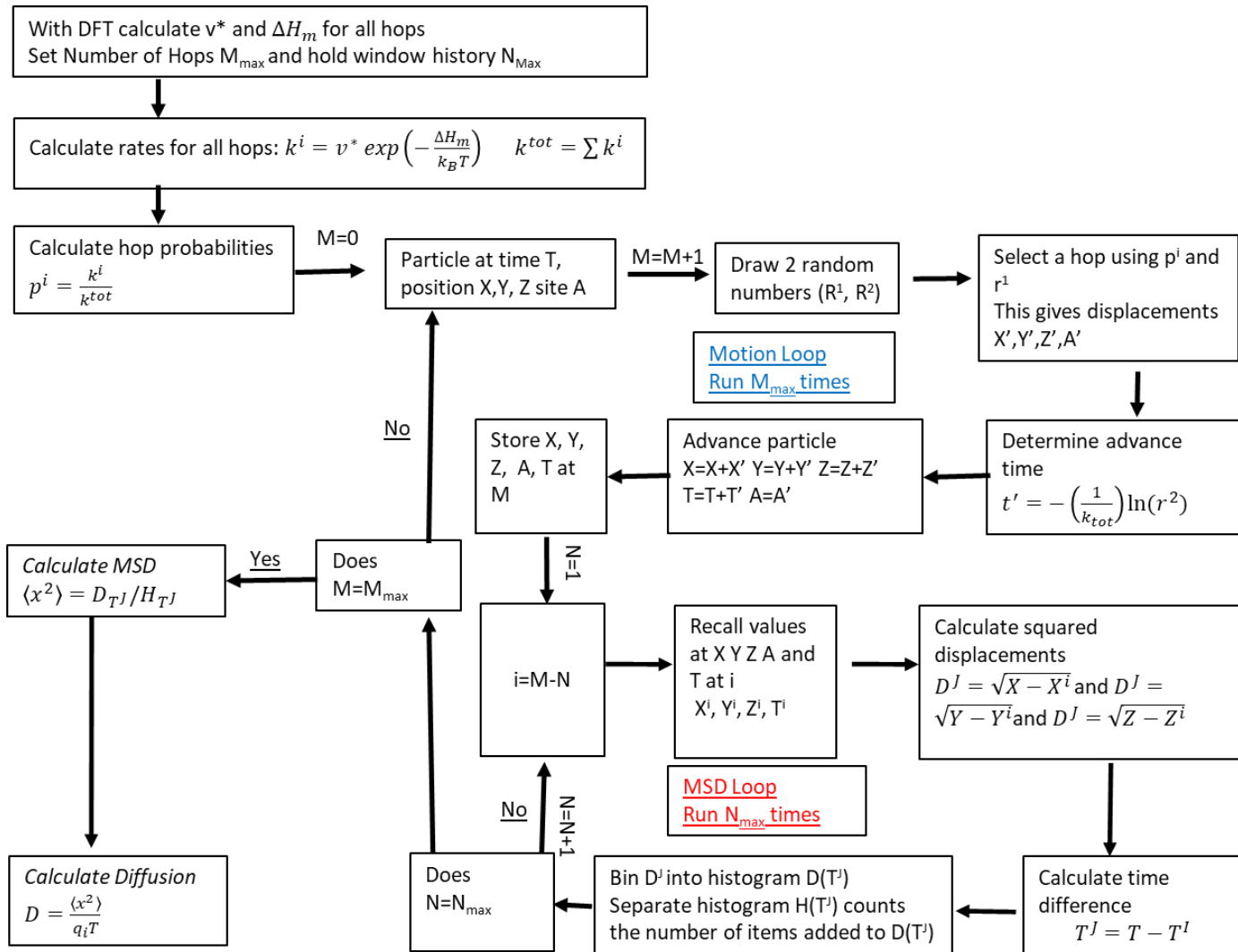


Figure S5: Flow diagram showing the main logic of the MSD and KMC algorithm. There are two loops- the second MSD loop can be run either at the end after all motion steps have been calculated or simultaneously with the motion steps as shown here.

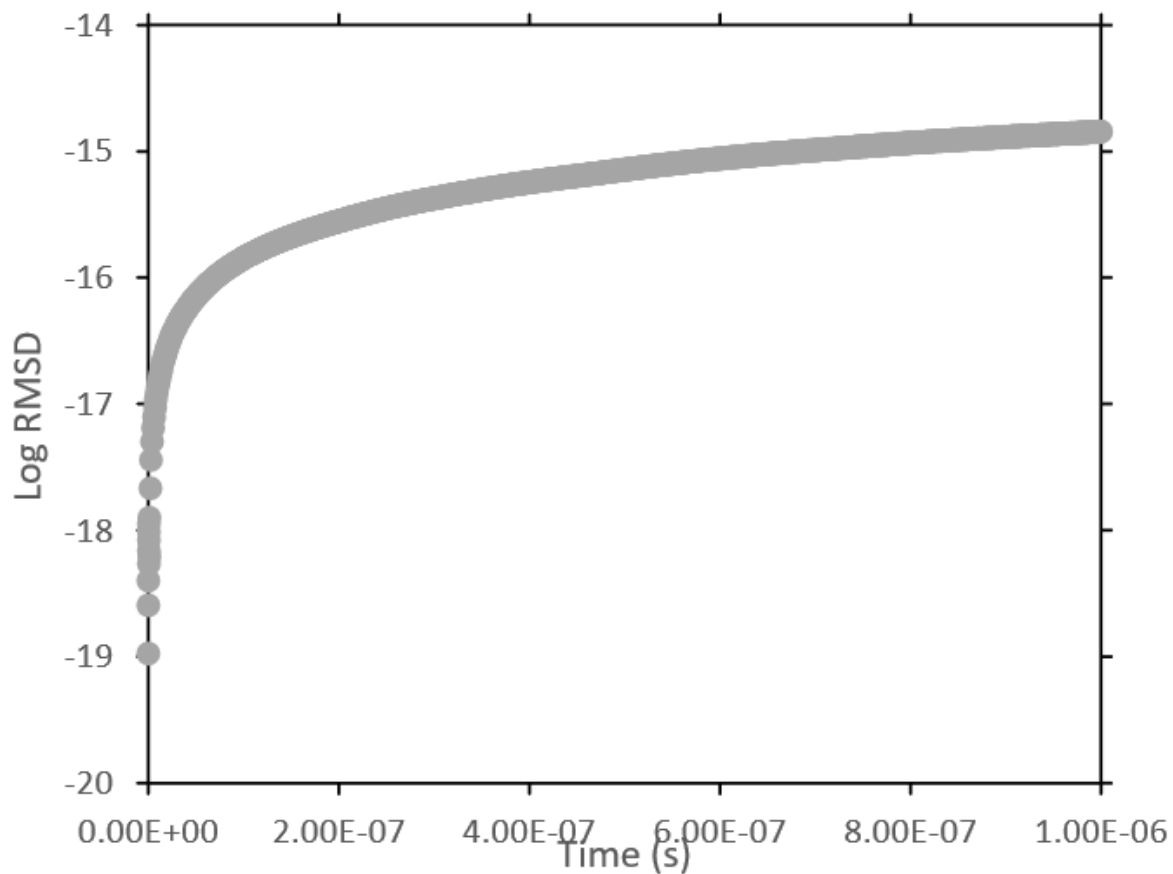


Figure S6: Sample graph showing the log of the RMSD against time for vacancy hopping in the [001] direction at 1300 K. Diffusion can be calculated by calculated the slope of the RMSD vs T. Diffusion is determined by the trend of the RMSD vs time but the earliest time steps (before a linear trend is reached) are discarded as diffusion is defined against the long-time limit.

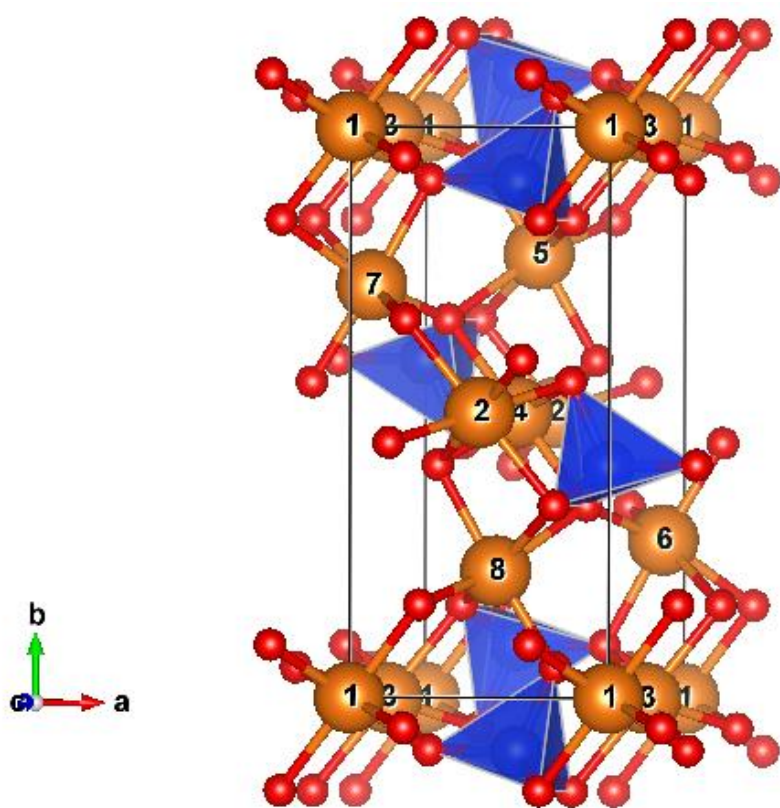


Figure S7: Unit cell of forsterite with labelled magnesium for reference in Table S4 and S8.

| P_{DFT} (GPa) | Vol_{DFT} (\AA^3) | $P_{\text{DFTCorrect}}$ (GPa) | P_{Exp} (GPa) | Vol_{Exp} (\AA^3) | $\text{Vol}_{\text{DFTCorrect}}$ (\AA^3) | E_{diff} (DFT- Experiment) (meV/atom) |
|---------------------------|---|----------------------------------|------------------------|---|--|--|
| 0 | 299.31 | -3.95 | 0 | 290.22 | 290.02 | -10.43 |
| 5 | 287.71 | 1.05 | 5 | 280.06 | 279.91 | -8.87 |
| 10 | 278.08 | 6.05 | 10 | 271.13 | 271.61 | 32.89 |

Table S1: List of theoretical unit cell volumes determined at 0, 5 and 10 GPa and the corrected pressure of these runs. We also list experimental unit cell volumes from Downs et al. (1996) and the predicted unit cell volumes of our DFT calculations once our pressure correction is applied. The difference between these corrected DFT volumes and the experimental volumes is listed as a function of energy and is small.

| | | 0 GPa | 5 | 10 |
|------------|----|-------|------|------|
| V''_{Mg} | M1 | 0 | 0 | 0 |
| | M2 | 0.88 | 1.12 | 1.20 |
| Mg_{int} | M1 | -0.2 | 0.00 | 0.16 |
| | I2 | 0 | 0 | 0 |

Table S2: Relative enthalpy (in eV/defect) of anhydrous and hydrous M1 and M2 vacancies and of anhydrous M1 and I2 interstitials. All pressures are uncorrected.

| | 5 GPa | | | 10 GPa | | | 15 GPa | | |
|----|--------|-------|-------|--------|-------|-------|--------|-------|-------|
| | 1000 K | 1500 | 2000 | 1000 K | 1500 | 2000 | 1000 K | 1500 | 2000 |
| R1 | 5.96 | 5.66 | 5.37 | 6.37 | 6.18 | 5.94 | 6.92 | 6.88 | 6.75 |
| R2 | 7.36 | 7.27 | 7.17 | 8.45 | 8.53 | 8.54 | 9.53 | 9.79 | 9.95 |
| R3 | 8.81 | 8.86 | 9.06 | 9.02 | 9.22 | 9.55 | 9.26 | 9.59 | 10.03 |
| R4 | 4.54 | 4.21 | 3.97 | 4.27 | 3.73 | 3.28 | 3.93 | 3.17 | 2.51 |
| R5 | 17.14 | 15.97 | 15.08 | 17.93 | 16.78 | 15.81 | 18.24 | 17.39 | 16.47 |
| R6 | 20.83 | 21.60 | 23.19 | 27.86 | 28.03 | 28.84 | 35.97 | 35.65 | 35.82 |

Table S3: Energy (eV/f.u.) of Reactions R1-R6 at various uncorrected pressures and temperatures

| Site | [100] | [010] | [001] | Degeneracy | Hops between sites starting from 1/5 | Possible Directions from Sites 1/5 |
|---------------------------|-------|-------|-------|------------|--------------------------------------|--|
| Vacancy Hops from M1 | | | | | | |
| A | 0.000 | 0.000 | 0.500 | 2 | 1-3 | +c,-c |
| B | 1.000 | 0.000 | 0.000 | 2 | 1-1 | +a,-a |
| C | 0.009 | 0.277 | 0.250 | 2 | 1-6/7 | -a +b +c, +a -b -c |
| D | 0.491 | 0.223 | 0.250 | 2 | 1-5/8 | -a -b +c, +a +b -c |
| D* | 0.509 | 0.223 | 0.250 | 2 | 1-5/8 | +a -b +c, -a +b -c |
| Vacancy Hops From M2 Site | | | | | | |
| C | 0.009 | 0.277 | 0.250 | 2 | 5-2/4 | -a -b -c, -a -b +c |
| D | 0.491 | 0.223 | 0.250 | 2 | 5-1/3 | +a +b -c, +a +b +c |
| D* | 0.509 | 0.223 | 0.250 | 2 | 5-1/3 | -a +b -c, -a +b +c |
| E | 0.500 | 0.055 | 0.500 | 4 | 5-7 | +a -b +c, +a -b -c, -a -b +c, -a -b -c |
| F | 1.000 | 0.000 | 0.000 | 2 | 5-5 | +a,-a |

Table S4: List of different vacancy hops and their absolute hop distance in unit cell values (at 0 GPa uncorrected these are 4.80, 10.32 and 6.04 Å respectively) and their degeneracy. To illustrate the degeneracy of the hops we have shown the possible hops between different sites and the different degenerate directions with hops starting from site 1 (an M1 site) and from site 5 (an M2 site) (with atom labels in Figure S7).

| | | Vacancy Hops | | |
|------|----------|--------------|------|--------|
| | Distance | Walker | Gulp | CASTEP |
| A | 2.99 | 0.72 | 0.77 | 0.75 |
| C-M1 | 3.26 | 1.96 | 2.10 | 1.45 |
| C-M2 | 3.26 | 0.06 | 0.19 | 0.45 |
| D-M1 | 3.58 | 4.54 | 2.28 | 1.99 |
| D-M2 | 3.58 | 6.64 | 0.37 | 1.00 |
| E | 3.89 | 1.47 | 2.53 | 1.63 |
| B | 4.78 | 5.89 | 6.06 | 4.12 |
| F | 4.78 | 9.1 | 3.96 | 2.82 |

Table S5: Comparison of vacancy hopping activation energies from forcefield calculations in literature (Walker *et al.* 2010) and with our DFT CASTEP calculations and additional calculations done with the TBH1 forcefield. All calculations are at 0 GPa uncorrected. For asymmetrical hops the starting site of the hop is listed. Hop distances are in Å and activation energies in eV.

| | | 0 GPa | 5 | 10 |
|-------------------|--------|-------|------|------|
| Hops From M1 Site | | | | |
| A | M1-M1 | 0.75 | 0.75 | 0.75 |
| B | M1-M1 | 4.12 | 4.29 | 4.63 |
| C | M1-M2/ | 1.45 | 1.52 | 1.63 |
| D | M1-M2/ | 1.99 | 1.92 | 1.85 |
| D* | M1-M2/ | 1.99 | 1.92 | 1.85 |
| Hops From M2 Site | | | | |
| C | M2-M1 | 0.45 | 0.45 | 0.47 |
| D | M2-M1 | 1.00 | 0.84 | 0.69 |
| D* | M2-M1 | 1.00 | 0.84 | 0.69 |
| E | M2-M2 | 1.63 | 1.72 | 2.00 |
| F | M2-M2 | 2.87 | 2.97 | 3.30 |

Table S6: Variation in activation energy (in eV) of vacancy hops with uncorrected pressure

| | | Vacancy | | | Interstitial | | |
|-------------------------------|-------|----------------------------|----------------------------|----------------------------|----------------------------|----------------------------|----------------------------|
| | | 0 GPa | 5 | 10 | 0 GPa | 5 | 10 |
| Hops from M1 Site | A/G | 1.01 X 10 ¹³ | 1.08 X 10 ¹³ | 1.23 X 10 ¹³ | 9.11 X 10 ⁸ | 9.70 X 10 ⁸ | 1.11 X 10 ⁹ |
| | B/H | 3.71 X 10 ¹⁵ | 2.95 X 10 ¹⁵ | 2.36 X 10 ¹⁵ | 1.22 X 10 ¹⁰ | 9.52 X 10 ⁹ | 7.71 X 10 ⁹ |
| | C/I | 2.37 X 10 ¹⁴ | 2.43 X 10 ¹⁴ | 2.57 X 10 ¹⁴ | 3.01 X 10 ⁹ | 3.08 X 10 ⁹ | 3.26 X 10 ⁹ |
| | I* | | | | 2.38 X 10 ⁸ | 2.44 X 10 ⁸ | 2.64 X 10 ⁸ |
| | D/J | 4.39 X 10 ¹⁴ | 4.43 X 10 ¹⁴ | 4.59 X 10 ¹⁴ | 2.02 X 10 ⁹ | 2.04 X 10 ⁹ | 2.14 X 10 ⁹ |
| | D*/J* | 4.39 X 10 ¹⁴ | 4.43 X 10 ¹⁴ | 4.59 X 10 ¹⁴ | 2.80 X 10 ⁹ | 2.83 X 10 ⁹ | 2.96 X 10 ⁹ |
| Hops From M2/I2 Site | C/I | 1.15 X 10 ¹⁴ | 1.51 X 10 ¹⁴ | 2.07 X 10 ¹⁴ | 1.41 X 10 ¹³ | 1.85 X 10 ¹³ | 2.53 X 10 ¹³ |
| | I* | | | | 1.11 X 10 ¹² | 1.46 X 10 ¹² | 2.00 X 10 ¹² |
| | D/J | 2.13 X 10 ¹⁴ | 2.70 X 10 ¹⁴ | 3.36 X 10 ¹⁴ | 9.46 X 10 ¹² | 1.20 X 10 ¹³ | 1.49 X 10 ¹³ |
| | D*/J* | 2.13 X 10 ¹⁴ | 2.70 X 10 ¹⁴ | 3.36 X 10 ¹⁴ | 1.31 X 10 ¹³ | 1.66 X 10 ¹³ | 2.07 X 10 ¹³ |
| | E/K | 4.27 X 10 ¹⁴ | 4.91 X 10 ¹⁴ | 5.73 X 10 ¹⁴ | 5.53 X 10 ¹² | 6.36 X 10 ¹² | 7.41 X 10 ¹² |
| | F/L | 2.31 X 10 ¹⁵ | 2.10 X 10 ¹⁵ | 1.85 X 10 ¹⁵ | | | |

Table S7: Attempt Frequency of the various hops in Hz as a function of uncorrected pressure

| Site | [100] | [010] | [001] | Degeneracy | Hops between sites starting from 1/13 | Possible Directions from Sites 1/13 |
|----------------------------|-------|-------|-------|------------|---------------------------------------|--|
| Interstitial sites from M1 | | | | | | |
| G | 0.000 | 0.000 | 0.500 | 2 | 1-3 | +c,-c |
| H | 1.000 | 0.000 | 0.000 | 2 | 1-1 | +a,-a |
| I | 0.009 | 0.277 | 0.250 | 2 | 1-13/16 | -a +b -c, +a -b +c |
| I* | 0.009 | 0.277 | 0.250 | 2 | 1-14/15 | -a -b -c, +a +b +c |
| J | 0.491 | 0.223 | 0.250 | 2 | 1-14/15 | +a -b -c, -a +b +c |
| J* | 0.509 | 0.223 | 0.250 | 2 | 1-3 | +c,-c |
| Interstitial Hops from I2 | | | | | | |
| I | 0.009 | 0.277 | 0.250 | 2 | 13-1/3 | -a +b -c, -a +b +c |
| I* | 0.009 | 0.277 | 0.250 | 2 | 13-2/4 | +a -b +c, +a -b -c |
| J | 0.491 | 0.223 | 0.250 | 2 | 13-2/4 | -a -b +c, -a -b -c |
| J* | 0.509 | 0.223 | 0.250 | 2 | 13-15 | +a -b +c, +a -b -c, -a -b +c, -a -b -c |
| K | 0.500 | 0.055 | 0.500 | 4 | 13-13 | +a,-a |
| L | 1.000 | 0.000 | 0.000 | 2 | 13-1/3 | -a +b -c, -a +b +c |

Table S8: List of different interstitial hops and their absolute hop distance in unit cell values (at 0 GPa uncorrected these are 4.800, 10.32 and 6.04 Å respectively) and their degeneracy. As I2 sites are simply M2 sites shifted by 0.5 in the A direction these hops are the same as the vacancy hops but M1-I2 hops go in different relative directions than M1-M2 hops. To illustrate the degeneracy of the hops we have shown the possible hops between different sites and the different degenerate directions with hops starting from site 1 (an M1 site) and from site 13 (an I2 site) (with atom labels in Figure S7).

| | 0 GPa | 5 | 10 |
|-------------------|-------|------|------|
| Hops from M1 Site | | | |
| G | 3.22 | 3.05 | 2.88 |
| H | 3.16 | 3.27 | 3.38 |
| I | 0.59 | 0.28 | 0.01 |
| I* | 1.35 | 0.99 | 0.63 |
| J | 0.56 | 0.39 | 0.21 |
| J* | 1.29 | 0.81 | 0.32 |
| Hops from I2 site | | | |
| I | 0.39 | 0.29 | 0.17 |
| I* | 1.15 | 1.00 | 0.84 |
| J | 0.36 | 0.36 | 0.36 |
| J* | 1.09 | 0.78 | 0.47 |
| K | 1.08 | 1.42 | 1.78 |

Table S9: Variation in Activation Energy (in eV) of interstitial hops with uncorrected pressure.

| | | [100] | [010] | [001] |
|----------------------|--------|------------------------|------------------------|------------------------|
| Anhydrous vacancy | 1000 K | 3.92×10^{-14} | 1.6×10^{-13} | 1.88×10^{-10} |
| | 1300 | 9.96×10^{-12} | 3.00×10^{-11} | 1.27×10^{-09} |
| | 1600 | 3.30×10^{-10} | 8.68×10^{-10} | 5.30×10^{-09} |
| Interstitial | 1000 | 2.94×10^{-12} | 1.16×10^{-11} | 6.13×10^{-12} |
| | 1300 | 7.48×10^{-12} | 2.87×10^{-11} | 1.39×10^{-11} |
| | 1600 | 1.53×10^{-11} | 5.55×10^{-11} | 2.46×10^{-11} |

Table S10: Diffusion coefficients (m^2/s) of vacancies and interstitials in three directions at 5 GPa uncorrected.

| | | [100] | [010] | [001] |
|----------------------|--------|------------------------|------------------------|------------------------|
| Anhydrous vacancy | 1000 K | 7.95×10^{-14} | 2.11×10^{-13} | 1.88×10^{-10} |
| | 1300 | 1.72×10^{-11} | 4.16×10^{-11} | 1.19×10^{-09} |
| | 1600 | 4.86×10^{-10} | 1.07×10^{-09} | 4.93×10^{-09} |
| Interstitial | 1000 | 2.04×10^{-11} | 9.05×10^{-11} | 6.66×10^{-11} |
| | 1300 | 3.66×10^{-11} | 1.49×10^{-10} | 8.44×10^{-11} |
| | 1600 | 5.87×10^{-11} | 2.18×10^{-10} | 1.01×10^{-10} |

Table S11: Diffusion coefficients (m^2/s) of vacancies and interstitials in three directions at 10 GPa uncorrected.

| | | 0 GPa | | | 5 GPa | | | 10 GPa | | |
|----------------------|--------|------------------------|------------------------|------------------------|------------------------|------------------------|------------------------|------------------------|------------------------|------------------------|
| | | [100] | [010] | [001] | [100] | [010] | [001] | [100] | [010] | [001] |
| Anhydrous Vacancy | 1000 K | 6.28×10^{-27} | 3.20×10^{-26} | 7.76×10^{-23} | 1.20×10^{-28} | 5.01×10^{-28} | 5.76×10^{-25} | 7.33×10^{-30} | 1.95×10^{-29} | 1.73×10^{-26} |
| | 1300 | 2.87×10^{-21} | 1.21×10^{-20} | 1.26×10^{-18} | 8.78×10^{-23} | 2.64×10^{-22} | 1.12×10^{-20} | 1.62×10^{-23} | 3.90×10^{-23} | 1.11×10^{-21} |
| | 1600 | 8.78×10^{-18} | 3.86×10^{-17} | 5.48×10^{-16} | 7.07×10^{-19} | 1.86×10^{-18} | 1.13×10^{-17} | 1.40×10^{-19} | 3.08×10^{-19} | 1.42×10^{-18} |
| Interstitial | 1000 | 1.43×10^{-25} | 3.13×10^{-25} | 1.10×10^{-25} | 8.98×10^{-27} | 3.55×10^{-26} | 1.87×10^{-26} | 1.88×10^{-27} | 8.35×10^{-27} | 6.14×10^{-27} |
| | 1300 | 1.19×10^{-21} | 3.08×10^{-21} | 1.01×10^{-21} | 6.59×10^{-23} | 2.53×10^{-22} | 1.22×10^{-22} | 3.43×10^{-23} | 1.40×10^{-22} | 7.91×10^{-23} |
| | 1600 | 3.68×10^{-19} | 7.54×10^{-19} | 3.80×10^{-19} | 3.28×10^{-20} | 1.19×10^{-19} | 5.27×10^{-20} | 1.70×10^{-20} | 6.31×10^{-20} | 2.91×10^{-20} |
| Combined | 1000 | 1.50×10^{-25} | 3.45×10^{-25} | 7.77×10^{-23} | 9.10×10^{-27} | 3.60×10^{-26} | 5.94×10^{-25} | 1.89×10^{-27} | 8.37×10^{-27} | 2.35×10^{-26} |
| | 1300 | 4.06×10^{-21} | 1.51×10^{-20} | 1.26×10^{-18} | 1.54×10^{-22} | 5.17×10^{-22} | 1.13×10^{-20} | 5.04×10^{-23} | 1.79×10^{-22} | 1.19×10^{-21} |
| | 1600 | 9.14×10^{-18} | 3.93×10^{-17} | 5.48×10^{-16} | 7.39×10^{-19} | 1.98×10^{-18} | 1.14×10^{-17} | 1.57×10^{-19} | 3.71×10^{-19} | 1.45×10^{-18} |

Table S12: Diffusion rates (m^2/s) of vacancies, interstitials and their combined diffusion rate at various uncorrected pressures and temperatures for anhydrous forsterite.

| Atoms | | | |
|---------------------------------------|----------------------------|-------------------------|-------------------------------|
| | q_{core} (eV) | q_{shell} (eV) | |
| Mg | 2.0 | n/a | |
| Si | 4.0 | n/a | |
| O | 0.84819 | 2.84819 | - |
| O _H | -1.426 | n/a | |
| H | 0.426 | n/a | |
| Buckingham Potential | | | |
| | A (eV) | ρ (Å) | C_{ij} (eV*Å ⁶) |
| Mg-O | 1428.5 | 0.29435 | 0 |
| Mg-O _H | 1060.5 | 0.29435 | 0 |
| Si-O | 1283.907 | 0.32052 | 10.66158 |
| Si-O _H | 983.556 | 0.32052 | 10.66128 |
| O*-O* | 22764 | 0.149 | 27.88 |
| O*-H ^b | 311.96 | 0.25 | 0 |
| Morse | | | |
| | D_e (eV) | A (Å ⁻¹) | r_0 (Å) |
| H-OH | 7.02525 | 2.03 | 0.9485 |
| Three Body | | | |
| | k3 (eV rad ⁻²) | Θ_0 (°) | |
| O*-Si-O* | 2.0972 | 109.47 | |
| Spring | | | |
| | k2 (eV Å ⁻²) | | |
| O _{core} -O _{shell} | 74.92038 | | |

Table S13: Potentials used in our forcefields calculations. O (the normal oxygen in the crystal lattice) and O_H (the oxygen in a hydroxyl group) have some unique but also some shared forcefields- O* represents both O and O_H. The Morse potential for O_H-H interactions was set to operate between 0 and 1.5 Å whereas the Buckingham potential for O-H interactions was set to operate between 1.5-10 Å. This ensures (with a sensible starting geometry) that the O-H bond is modelled by a Morse potential but the interaction of the oxygen in the OH group with the other Hydrogen in the vacancy is modelled with a Buckingham potential. If both potentials are set to operate from 0- 10 Å then the hydrogen atoms either fall outside of the vacancy or into the centre of the vacancy (depending upon starting geometry) which does not match the more accurate predictions of DFT.